Negative microfilm received from university

64–8167

GROBLICKI, Peter John, 1938–
ATOMIC BEAM SCATTERING STUDIES ON THE Li–Hg SYSTEM: VELOCITY DEPENDENCE OF TOTAL AND DIFFERENTIAL CROSS SECTIONS AS A ROUTE TO THE INTERACTION POTENTIAL.

The University of Michigan, Ph.D., 1963
Chemistry, physical

University Microfilms, Inc., Ann Arbor, Michigan

ATOMIC BEAM SCATTERING STUDIES ON THE Li-Hg SYSTEM: VELOCITY DEPENDENCE OF TOTAL AND DIFFERENTIAL CROSS SECTIONS AS A ROUTE TO THE INTERACTION POTENTIAL

by

PETER JOHN GROBLICKI

A dissertation submitted in partial fulfillment
of the requirements for the degree of
Doctor of Philosopy in the
University of Michigan
1963

Doctoral Committee:

Professor Richard B. Bernstein, Co-chairman
Professor Lawrence O. Brockway, Co-chairman
Assistant Professor Peter R. Fontana
Assistant Professor Adon A. Gordus
Professor Joseph O. Halford

ACKNOWLEDGEMENTS

The author would like to express his sincere thanks to all who have contributed advice or material support to this investigation.

It has been a pleasure to work under the supervision of Professor R.B. Bernstein; his knowledge, suggestions and aid have contributed immeasurably to the success of this project.

The apparatus was constructed by Dr. H. U. Hostettler; its operation and idiosyncrasies were explained to the author by Dr. F.A. Morse. Drs. A. R. Blythe, A. E. Grosser, H. Harrison and K. H. Kramer have provided many stimulating conversations. The services of C. Charters, G. Franz, A. Graube, N. Johnston, A. Korreck, and F. Parker are gratefully acknowledged.

Financial support was received from the U.S. Atomic Energy Commission under Contracts AT (11-1)-321 (Univ. of Michigan) and AT (11-1)-1328 (Univ. of Wisconsin). Partial support for some of the computations carried out at the University of Wisconsin was obtained through N.A.S.A. Grant NsG-275-62. The author was the holder of a University of Michigan Teaching Fellowship, a National Science Foundation Cooperative Graduate Fellowship and a Minnesota Mining and Manufacturing Company Fellowship, which are acknowledged with thanks.

Finally, the aid of his wife, Lois, must be acknowledged; not only for assistance in the preparation of the thesis, but also for her continued encouragement and understanding.

TABLE OF CONTENTS

		Page
I.	Introduction	
	A. Molecular Beam Scattering	1
	B. Theoretical Predictions of Total and Differential Cross Sections	1
	C. Experiments with Light Atom Systems	3
II.	Experimental Details	
	A. Apparatus	5
	B. Geometry	6
	C. Materials	9
	D. Experimental Procedure	10
III.	Experimental Results	12
	A. Representations Suitable for Comparison with Theory	
	1. Differential Cross Sections	12
	2. Total Cross Sections	17
	B. Experimental Results	
	1. Differential Cross Sections	18
	2. Total Cross Sections	35
IV.	Theoretical Predictions and Comparison with Experimental Results	
	A. Differential Cross Sections	
	1. Calculation of Differential Cross Sections	39
	2. Comparison of Theory and Experimental Results	41
	B. Total Cross Sections	
	1. Calculation of Total Cross Sections	56
	2. Comparison of Theory and Experimental Results	58

V. Discussion 60

VI. Summary 65

APPENDICES

A. Phase Shifts Calculated by the Exact Method 67

B. Comparison of Semiclassical and Quantum Total Cross Sections 74

C. Transistorized Temperature Regulator 76

REFERENCES 79

LIST OF TABLES

Table		Page
I.	Apparatus Dimensions	7
II.	Angular Positions of Undulations in Experimental $G(\theta)$ Curves	33
III.	Angular Positions of Maxima and Minima in Theoretical $G^*(\theta)$ Curves (at various values of B)	
	a. 1000	44
	b. 1500	45
	c. 1500	46
	d. 2000	47
	e. 2000	48
IV.	Potential Parameters Determined from Angular Distributions	52
V.	Parameters Obtained Using Data on Total Cross Sections as well as Angular Distributions	59
VI.	Vibrational Level Capacity of L.-J. (12,6) Potential Wells	61
VII.	Summary of Experimental Results	62
VIII.	Values of C_{exp} Based on Experimental ϵ , σ Values	63
IX.	Comparisons of Phase Shifts	67

X. Calculated Phase Shifts (at various values of B)

a. 1000 68

b. 1500 69

c. 1500 70

d. 1500 71

e. 2000 72

f. 2000 73

LIST OF FIGURES

Figure		Page
1.	Li Beam Geometry: Top View	8
2.	Collision Geometry	14
3.	Typical Original Data: Angular Distributions	19
4.	Typical Data: Center of Mass Presentation	21
5.	Log-log Plot of C.M. Data from Fig. 4	22
6.	Typical Data: G(θ) Presenation	23
7.	Experimental Data: Li^6-Hg at various v_r:	
	a. 784 m/s	24
	b. 1140 m/s	25
	c. 1213 m/s	26
8.	Experimental Data: Li^7-Hg at various v_r:	
	a. 697 m/s	27
	b. 784 m/s	28
	c. 979 m/s	29
	d. 1032 m/s	30
	e. 1140 m/s	31
	f. 1213 m/s	32
9.	Summary of Experimental Scattering Patterns	34
10.	Typical Original Data on Li Beam Attenuation	36
11.	Total Cross Section Data: Li^6-Hg	37
12.	Total Cross Section Data: Li^7-Hg	38
13.	Comparison of $I^*(\theta)$ and $G^*(\theta)$ presentations	42
14.	Typical Family of $G^*(\theta)$ Curves	43
15.	Scattering Patterns at various B:	
	a. 1000	49

b. 1500 50
c. 2000 51

16. Comparison of Theoretical and Experimental Scattering Patterns at various B:
a. 1000 53
b. 1500 54
c. 2000 55

17. Patterns of the Extrema in Total Cross Sections 57
18. Comparison of Semiclassical and Quantum Cross Sections 75
19. Temperature Regulator 77

I. Introduction

A. Molecular Beam Scattering

Recent advances in experimental and theoretical techniques have made possible utilization of the molecular beam scattering technique to obtain meaningful information concerning intermolecular interactions. The development and application of compact, wide range velocity selectors, improved beam detection sensitivity due to modulation and phase-sensitive detection methods, and modern vacuum techniques have made many experiments possible. In addition, scattering measurements and the interaction potential are now more closely linked due to recent computational developments allowing ready calculation of total and differential cross sections from assumed potentials. Recent pertinent reviews include Bernstein (in press), Fite and Datz (1963), and Pauly (1961).

B. Theoretical Predictions of Total and Differential Cross Sections

The semiclassical model provides an adequate description of scattering in heavy particle systems, but quantum mechanics is required to treat collisions involving a particle of low mass where the deBroglie wavelength λ of the system is of the order of atomic dimensions. Mott and Massey (1949) have outlined the partial wave method in which the scattering of an incident plane wave by a static central potential is considered as the sum of contributions from a set of "partial waves", each corresponding to a different incoming partial wave with angular momentum quantum number l . Associated

with each ℓ is the so-called scattering phase shift η_ℓ arising due to the presence of the potential. A set of phase shifts $\eta_\ell(k)$ is required for any given wave number k ($k=2\pi/\lambda = \mu v/\hbar$, where μ is the reduced mass of the system and v is the initial relative velocity) and potential energy function.* Bernstein (1960, 1961) has developed procedures for the numerical solution of the one-dimensional radial wave equation involving the potential which yield the scattering phase shifts. From these phases, the total cross section Q (sometimes called σ) and the differential cross section $I(\theta) = d\sigma(\theta)/d\omega$ can be evaluated (Mott and Massey, 1949):

$$Q(k) = \left(\frac{4\pi}{k^2}\right) \sum_\ell (2\ell+1) \sin^2 \eta_\ell(k) \qquad (1)$$

$$I(\theta) = \frac{1}{4k^2} \left\{ \left[\sum_\ell (2\ell+1) \sin 2\eta_\ell P_\ell(\cos\theta) \right]^2 + \left[\sum_\ell (2\ell+1) (\cos 2\eta_\ell - 1) P_\ell(\cos\theta) \right]^2 \right\} \qquad (2)$$

where P_ℓ is the Legendre function. Bernstein's calculations have predicted an oscillatory behavior (interferences) for the differential cross sections and extrema in the total cross sections, Q(v), when realistic potentials involving long range attraction and short range repulsion have been considered.

- - - - - - - -

* Any realistic potential energy function requires the specification of at least two parameters, first, ϵ , the depth of the well, and second, σ , the position of the first zero of the potential function. (See, for example, Hirschfelder, Curtiss and Bird, 1954)

Bernstein (1962, 1963) has also carried out a semiclassical analysis of the extrema in total cross sections for atom-atom collisions. He showed that the presence of these extrema is related to the existence of bound (vibrational) states in the potential well. The positions of the extrema in Q(v) lead to an evaluation of the product $\epsilon\sigma$.

C. Experiments with Light Atom Systems

Hostettler and Bernstein (1960b) reported experimental results indicating the presence of deBroglie interferences in differential cross sections for the scattering of a monoenergetic Li beam by a crossed Hg beam. They also observed a maximum in Q(v), but did not resolve any additional extrema. They chose the Li-Hg system for this work because:

1. Li is light enough to have a deBroglie wavelength near 1Å at experimentally attainable velocities.
2. Beams of both could easily be produced from heated ovens.
3. Li could be detected with a surface ionization detector.
4. Both had negligible vapor pressure when condensed on liquid nitrogen cooled traps.

Rol and Rothe (1962), Rothe, Rol, Trujillo and Neynaber (1962), Rothe, Rol and Bernstein (1963) and Rothe, Neynaber, Scott, Trujillo and Rol (1963) have reported extrema in the total cross sections for several alkali-rare gas systems: Li-Xe, Li-Kr, Li-Ar, K-Xe and K-Kr.

This thesis reports a continuation and extension of the studies on the Li-Hg system. The experimental results are to be compared with theoretical predictions based upon a simple Lennard-Jones (12,6) potential:

$$V(r) = 4\epsilon \left[\left(\frac{\sigma}{r}\right)^{12} - \left(\frac{\sigma}{r}\right)^{6} \right] \quad , \qquad (3)$$

from which it should be possible to deduce a "best set" of potential

parameters describing the Li-Hg system. More important than obtaining a set of potential parameters for any specific system is the development and testing of methods for the analysis of scattering data for systems exhibiting quantum effects.

Isotopically pure beams of Li^6 or Li^7 were used in order to reduce the spread in velocity (and hence ℓ) due to the mixture of these isotopes occurring in natural Li. Theory suggests that the differential scattering cross section should depend upon the deBroglie wavelength, $\lambda = \frac{\hbar}{\mu v}$ of the colliding pair, and not upon the relative velocity alone. This prediction can be tested in a direct way: proper selection of the velocity of the isotopic Li beams allows comparison of scattering patterns at the same deBroglie wavelength.

II. Experimental Details

A. Apparatus

Measurements were performed using the molecular beam apparatus described by Hostettler and Bernstein (1960b), Morse (1962), and Morse and Bernstein (1962). Li and Hg beams are formed by thermal effusion through a slit in a heated chamber containing molten Li or Hg. The Li beam passes through a velocity selector (Hostettler and Bernstein, 1960a) and is modulated at 25 cycles per second. The Li beam is then collimated and intersects the Hg beam at right angles. The Li source, velocity selector, modulator, collimator and Hg beam source are mounted on a turntable which rotates about the intersection of the Li and Hg beams. This allows the stationary detector to be placed at any angle (in the plane of the two beams) with respect to the Li beam.

The Li beam is detected by conversion to ions by surface ionization on a hot, oxygenated filament.* The Li^+ ions are accelerated

- - - - - - - -

* A stream of oxygen is sprayed at the filament (92% Pt, 8% W, Sigmund Cohn #479) through a fine tube connected with an external resevoir. This caused a pressure rise in the detector chamber of less than 10^{-6} Torr.

through 5 Kv to the first dynode of a 12 stage Cu-Be electron multiplier, where they yield secondary electrons. The output of the electron multiplier is measured by a cathode follower and D.C. recorder or a 25 c/s narrow band amplifier and phase sensitive detector.

The apparatus as used was essentially that detailed by Morse (1962) with small changes as follows: The Li oven slit was widened in order to increase the intensity. The Hg oven slit and collimator were narrowed, and the oven slit was packed with "Zacharias crinkly foil" (King and Zacharias, 1956) to reduce cloud formation and the angular spread of the beam. The liquid nitrogen cooled shield around the Hg oven was improved, reducing the amount of scattering from Hg vapor not in the intersection volume of the two beams. A transistorized temperature controller was constructed and used to maintain the Hg oven at a constant temperature. (See Appendix C.)

B. Geometry

The important apparatus constants are given in Table I. The half widths of the source, collimator, detector, detector beam stop, umbra, half-intensity points (equivalent rectangular image) and penumbra are denoted respectively by: s,c,d,b,u,h,p; ℓ_{ij} is the distance from point i to point j; "t" designates the scattering center or target. In this notation,

$$u = \left| c + \frac{(c-s)\,y}{\ell_{sc}} \right| \tag{4}$$

$$p = c + \frac{(c+s)\,y}{\ell_{sc}} \tag{5}$$

and

$$h = \frac{u+p}{2} \tag{6}$$

where $y = \ell_{ct}$ or ℓ_{cd} is used for calculations at the target and detector respectively. Primed quantities replace their counterparts

TABLE I

Apparatus Dimensions

(All entries are in centimeters)

	Li Beam	Hg Beam		Li Beam	Hg Beam
s	0.0266	0.080	s'	0.300	0.318
c	0.0191	0.080	c'	0.300	0.318
d	0.0254		d'	0.300	
b	0.0315		b'	0.300	

	Target	Detector	Target		Target	Detector	Target
u	0.0163	|-0.0010|[a]	0.0800	u'	0.300	0.300	0.318
h	0.0262	0.0713	0.1002	h'	0.411	1.10	0.398
p	0.0360	0.1416	0.1203	p'	0.522	1.91	0.478

ℓ_{bd}	1.23	
ℓ_{sc}	10.95	1.27
ℓ_{cd}	29.35	
ℓ_{ct}	4.05	0.32
ℓ_{td}	25.3	

ΔV = Scattering Volume = 0.00836 cm^3

A_d = Detector Area = 0.030 cm^2

- - - - - - - -

[a] A negative value is listed, indicating that the "rays" defining the edges of the umbra have crossed the zero position. See Figure I.

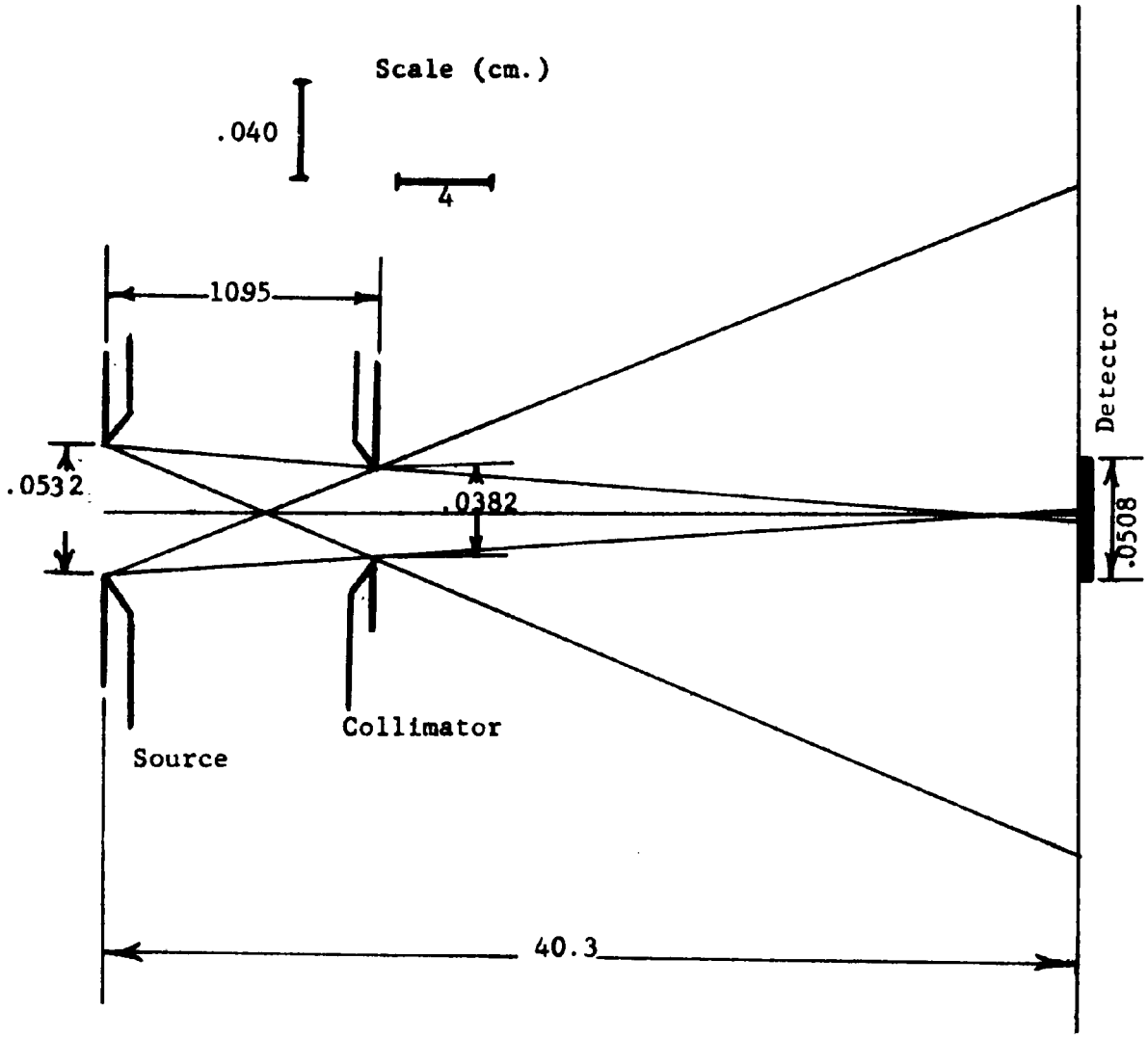


Figure 1: Li beam geometry: Top view. Note the different scales for length and width, also the "cross over" of the umbra.

in these equations when the half heights are desired.

The "nominal" or "geometrical" resolution angle is the angle which the detector subtends at the scattering center; for these experiments it was

$$\frac{2d}{\ell_{td}} = \frac{.0508 \text{ cm}}{25.3 \text{ cm}} = .002 \text{ radians or } 6.8' . \qquad (7)$$

This would be the smallest angle of scattering detectable in a "perfect" apparatus. Kusch (1960) has considered the effects of finite beam size on resolution and arrives at a criterion for an "effective" resolution angle, at which the efficiency of detection of scattering is 50%. The Kusch resolution angle for these experiments, for any $d < h$, where h refers to the primary beam at the detector, is

$$\frac{1.486\ h}{\ell_{td}} = .0042 \text{ radians} = 14.4'. \qquad (8)$$

The quantity G_A is a measure of the geometrical collection efficiency of the detector. $1/G_A$ is the fraction of beam molecules reaching the detector plane which is incident upon a detector of area less than the penumbra. This may be calculated from the detector dimensions and from the calculated (trapezoidal) intensity distribution in the detector plane. For these experiments, G_A was 3.1.

C. Materials

Mallinckrodt reagent grade mercury was used. The manufacturer claims less than 0.0006% total impurity.

Oak Ridge National Laboratories, suppliers of the Li^7 and Li^6 used,

furnished the following analysis of their material:
Isotopic purity: Li^7 99.994%, Li^6 0.01%; other elements less than 0.05% each, except Sr less than 0.2%.
Isotopic purity: Li^6 96.1%, Li^7 3.9%; other elements less than 0.05% each, except Ca and Zn, 0.25% or less.

D. Experimental Procedure

The alkali metal oven was loaded with pieces of Li (between 1.5 and 2 gm total) which had been rinsed with benzene. Benzene in the oven cavity prevented oxidation of the Li while the oven was assembled and installed in the apparatus. The benzene evaporated from the oven during the evacuation of the apparatus. When the diffusion pumps had reduced the pressure to 10^{-5} torr, the detector filament could be turned on to "boil out" alkali contamination.

When the vacuum (about 1×10^{-6} torr) and the background noise level from the filament were suitable, the ovens were brought to operating temperatures, heating slowly through the melting point of Li.

Within two hours of operation, the Li beam usually had become stable, and Hg was admitted to the scattering gas oven through a tube which allowed filling from outside the vacuum chamber. 0.5 cc lasted about one hour, and was replenished when necessary. Once the Hg oven had equilibrated, as judged by the constancy of its temperature and by a constant attenuation of the Li beam, measurements were made.

For total cross section measurements, a Li velocity was chosen, the signal was measured with the beam of Hg present, I, and with the beam of Hg interrupted by a shutter, I_o. This was repeated at various velocities of the Li beam. Measurements were considered valid only if those taken near the end of the series reproduced those taken at the beginning.

When angular distributions were desired, a transmission measurement was performed at zero degrees. Then the detector was placed at various angular positions with respect to the Li beam and the intensity measured in the presence of scattering gas. Usually, angles were chosen in a monotonic sequence, and only in the "Interior Quadrant". After the desired angular range had been covered, another measurement of the zero degree transmission was performed. Corrections for drift or background scattering were not applied. These small and necessarily somewhat arbitrary corrections would have a negligible effect on the location and resolution of the undulations. This procedure was repeated for each velocity and isotope. Most experiments were repeated on more than one day.

During a typical experiment, the temperature of the Li beam oven was maintained around $1100^{\circ}K$, the Hg beam oven was at $440^{\circ}K$, and I_o/I was in the range 1.1 to 1.7. At zero degrees, the unattenuated Li beam produced a current of about 10^{-7} amp at the collector of the electron multiplier, and a 1 volt signal at the output of the cathode follower. The gain of the electron multiplier varied between 10^3 and 10^4. Assuming 100% ionization efficiency and a 1:1 ion to electron conversion at the first dynode of the electron multiplier, the output signal corresponds to about 6×10^8 atoms per second striking the detector. The noise level was about 10^{-4} of the above signal, giving a detection sensitivity for Li of about 10^4 atoms per second, about two orders of magnitude poorer than for K or Cs in this apparatus. This lower sensitivity may be attributed to the increase in spurious alkali ion emission coming from the filament. Both the increased temperature of the surface ionization filament (1.1 amp heating current for Li, compared with 0.5 amp for K) and oxygenation of the filament cause much increased noise levels due to bursts of alkali ions given off by the filament (Minturn, Datz and Taylor, 1960).

III. Experimental Results

A. Representations Suitable for Comparison with Theory

1. Differential Cross Sections

Because theoretical predictions of differential scattering cross sections usually refer to the center of mass (CM) coordinate system, comparisons between theory and experiment are easiest if the experimental results are converted from measured angles, θ_a, and fluxes (number per unit time), F_a, in the laboratory or apparatus coordinate system (subscript a), to angles θ, and fluxes, F, in the CM system.

The CM conversion problem has been considered by Morse and Bernstein (1962) and by Morse (1962) where equations 9 to 22 are derived and discussed in more detail. Although the following material is not new, it is presented here for the purpose of defining the symbols and equations actually used in the analysis.

Associated with each type of particle is a velocity $\underline{v}_i$,*

- - - - - - - -

* This treatment assumes monoenergetic beams; in the present experiments, the Li beam has a velocity spread at half intensity of 4.7% of the nominal velocity, and the Hg beam has a Maxwellian distribution of velocities. Due to the heavy mass and consequently low average speed of the Hg, this introduces only a moderate spread in the relative velocity.

(and magnitude v_i) and a mass m_i. The vectors $\underline{v}_1$ (Li) and $\underline{v}_2$ (Hg), which intersect at $\psi = 90^o$, determine a plane. Figure 2 shows the geometrical relationship between the observed scattering angle θ_a and the CM deflection angle θ. Figure 2 applies to the present case of elastic scattering observed by a detector, sensitive only to Li, located in the plane of the incident beams, and restricted to the "Interior Quadrant". Also shown in Figure 2 are $\underline{v}_{CM}$, the velocity vector of the CM, and $\underline{w}_i$, the velocity vector of the i^{th} particle with respect to the CM. Primed quantities refer to "after the encounter".

For the special case of elastic scattering of perpendicularly intersecting beams, with the detector in the plane of the beams, the angles θ and θ_a are related by:

$$\theta = \arccos\left[\frac{2w_i^2 - v_i^2 - v_i'^2 + 2v_i v_i' \cos\theta_{a1}}{2w_i^2}\right]. \quad (9)$$

The magnitudes of the various terms may be calculated from:

$$w_i = w_i' = \frac{v_r m_2}{m_1 + m_2}, \quad (10)$$

$$v_r = \left(v_1^2 + v_2^2\right)^{\frac{1}{2}}, \quad (11)$$

$$v_i' = v_{CM}\cos\alpha_i' \pm \left(w_i^2 - v_{CM}^2 \sin^2\alpha_i'\right)^{\frac{1}{2}}, \quad (12)$$

$$v_{CM} = \left(w_i^2 + v_i^2 - \frac{2w_i v_i^2}{v_r}\right)^{\frac{1}{2}}, \quad (13)$$

$$\alpha_i' = \alpha_i - \theta_{a1}, \quad (14)$$

$$\text{and } \alpha_i = \arccos\left[\frac{v_{CM}^2 + v_i^2 - w_i^2}{2v_i v_{CM}}\right]. \quad (15)$$

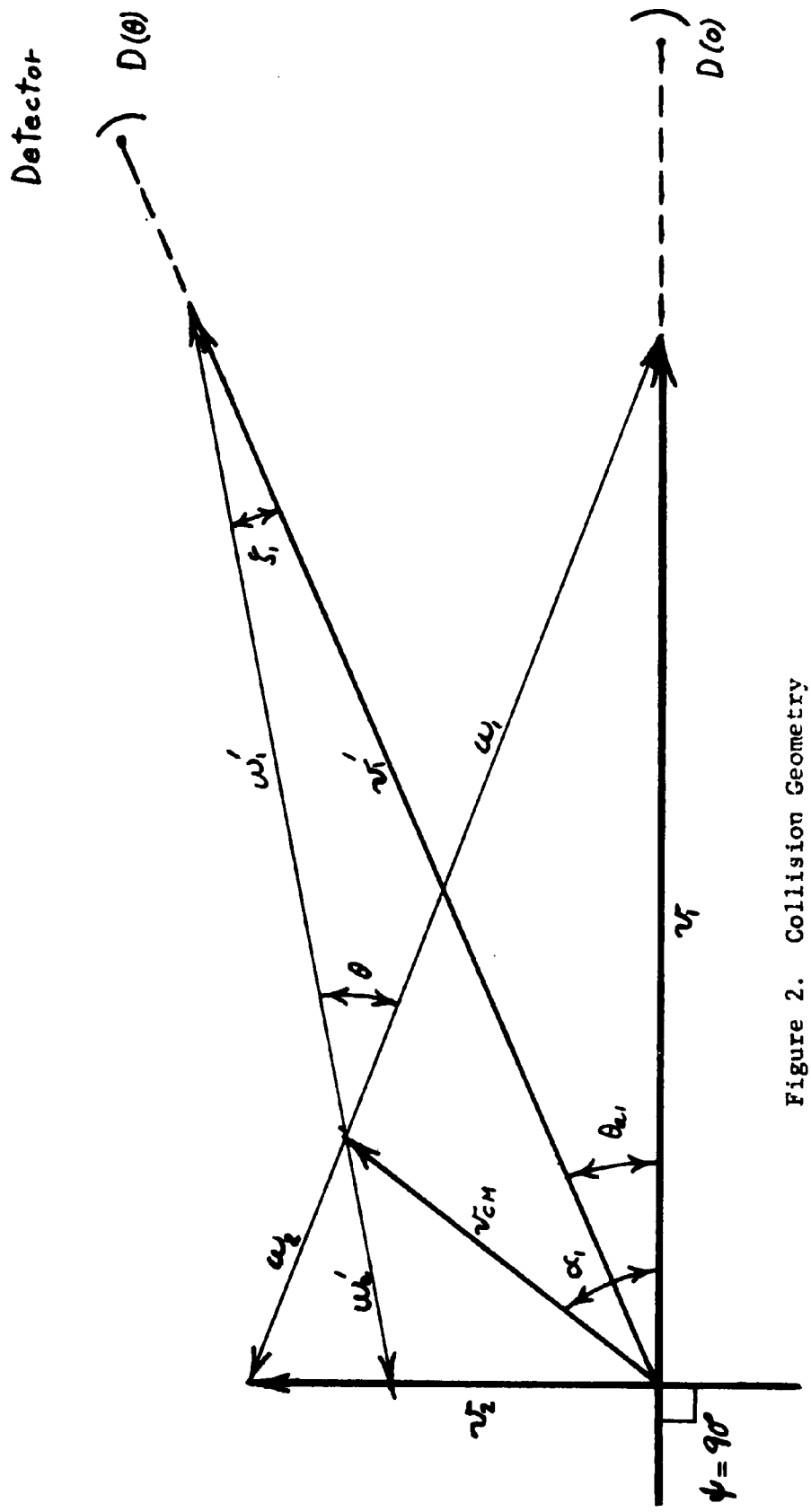


Figure 2. Collision Geometry
The relative velocity $\underline{v}_r = \underline{v}_1 - \underline{v}_2 = \underline{w}_1 - \underline{w}_2$ is not explicitly labelled.

The detector subtends different solid angles, $\Delta\omega_d$, in the CM and apparatus systems. The differential cross sections in the CM system, designated I(θ) or $\frac{d\sigma(\theta)}{d\omega}$ is related to the intensity of scattered particles measured by the detector by:

$$I_i(\theta_a) = \frac{\Delta F_i(\theta_a)}{\Delta \omega_d} = n_1 n_2 v_r \Delta V \frac{d\sigma_i(\theta_a)}{d\omega_a} \qquad (16)$$

$$I_i(\theta) = \frac{d\sigma(\theta)}{d\omega} = \frac{I_i(\theta_a)}{n_1 n_2 v_r \Delta V} \left(\frac{w_i}{v_i'}\right)^2 |\cos \xi_i| \,, \qquad (17)$$

$$\text{where} \qquad \cos \xi_i = \frac{w_i^2 + v_i'^2 - v_{cm}^2}{2 v_i' w_i} \qquad (18)$$

and n_i is the concentration of the i^{th} type particle in the scattering zone of volume ΔV. Appropriate averages over the concentrations in the scattering zone are performed, and, finally, the velocity dependence of the total cross section is removed. This requires the introduction of an assumed functional form for the velocity dependence of the total cross section. For the present purposes, Massey-Mohr behavior appropriate to an inverse sixth power attraction is used:

$$\sigma = \sigma_0 \; v^{-\frac{2}{5}} \qquad (19)$$

where σ_0 is given by

$$\sigma_0 = b C^{\frac{2}{5}} \quad ; \qquad (20)$$

here b is a known constant and C is the coefficient of the inverse sixth power attractive term. For the L.-J. (12,6) potential, this coefficient C is related to the potential parameters by

$$C = 4 \epsilon \sigma^6 \qquad (21)$$

An experimental quantity, closely related to the differential cross section, and which may be compared directly with theory, is then

defined as: $$D(\theta) \equiv \left[\frac{d\sigma(\theta)}{d\omega} \Big/ \sigma_o\right] \frac{G_A A_d}{\ell_{td}^2} \qquad (22a)$$

$$= \frac{F_1(\theta_a)}{\Delta S_1(0)} v_r^{-\frac{2}{5}} \left(\frac{w_1'}{v_1'}\right)^2 \left|\cos \zeta_1\right| . \qquad (22b)$$

Here $S_1(\theta) = \frac{F_1(\theta)}{G_A}$ is the signal observed at the detector at an angle θ, and $\Delta S_1(0)$ is the difference in primary beam signal, measured at zero degrees, due to the presence of the secondary beam in the scattering zone.

Both theoretical and experimental angular distributions show decreases in intensity of many orders of magnitude as the scattering angle is increased. Even if a semi-log plot of intensity versus angle is used, small effects such as undulations are difficult to observe in the presence of a rapidly changing "background". For a potential with a long range inverse sixth power dependence, the low angle scattering may be represented by (Kennard, 1938, pp. 119-120):

$$I(\theta) = \frac{\text{constant}}{\theta^{\frac{4}{3}} \sin\theta} \qquad (23a)$$

which for small angles becomes

$$I(\theta) \approx \text{constant} \cdot \theta^{-\frac{7}{3}} \qquad (23b)$$

Morse and Bernstein (1962) found angular distributions for the K- and Cs-Hg systems in agreement with this prediction. This suggests the utility of a new function,

$$G(\theta) = D(\theta) \cdot \theta^{\frac{7}{3}} \qquad (24)$$

which should be essentially constant at low angles, except where deviations from a smooth $\theta^{-7/3}$ dependence occur. This should allow detection of undulations with great sensitivity. This method of presentation has therefore been adopted in the present work.

After measurements of the scattered intensity are performed, the signal (partly masked by noise) appearing on the recorder charts must be converted to $G(\theta)$ values. This has been done objectively by the following procedure: An assistant* measures the position of the average value of the signal in arbitrary units. If the signal-to-noise ratio is poor, then three values are measured: the most likely, and the lowest and highest values of a possible "best reading". (These limits are thought to represent the 95% confidence level.) The attenuation at zero degrees is also measured in the same arbitrary units. The measured values are standardized by taking into account amplifier gain, and punched cards are prepared bearing a table of the intensity as a function of scattering angle θ_a. These tables, together with v_{Li}, T_{Hg} (from which $\bar{v}_{Hg}$ is calculated, as in the next section), and $\Delta S_1(0)$ are used with a program (utilizing equations 9 to 24) written for an IBM 7090 Computer to yield calculated values of θ, $D(\theta)$, and $G(\theta)$. Computing time for the 35 sets of data was less than 2 minutes.

2. Total Cross Sections

The goal of total cross section measurements is the absolute value of the total cross section, Q, which is related to the experimentally measured attentuation by:

$$Q(v_1) = \frac{\ln (I_0/I)}{F n_2 \ell} \qquad (25)$$

Here F is a function averaging over the distribution of relative velocities (Berkling, Helbing, Kramer, Pauly, Schlier, and Toschek, 1962). In crossed beam experiments, it is difficult to evaluate the product $n_2 \ell$ and thus the absolute total cross section Q. This problem

- - - - - - - -

* The diligence of Frank Parker, Catherine Charters, and Andrew Graube in making these measurements is greatly appreciated.

may be partially circumvented by defining a relative total cross section q as

$$q(\bar{v}_r) = \log\left(I_0/I\right) \frac{v_1}{\bar{v}_r} \qquad (26)$$

where $\bar{v}_r$ is an average relative velocity approximated by

$$\bar{v}_r = \left(v_1^2 + \bar{v}_2^2\right)^{\frac{1}{2}} \qquad (27)$$

where

$$\bar{v}_2 = 1.33\,\alpha_2 = 1.33\sqrt{\frac{2kT_2}{m_2}} \quad . \qquad (28)$$

The ratio $v_1/\bar{v}_r$ is approximately the function 1/F in Equation 25. If the Hg beam flux is maintained constant, then q is proportional to $Q(v_r)$.

A suitable presentation for total cross section data is a plot of $v_r^{2/5} \cdot Q(v_r)$ versus $1/v_r$ (Bernstein, 1963). The experimental results are presented as log-log plots of $v^{2/5} \cdot q$ versus 1/v where for brevity, we replace $\bar{v}_r$ by v. The logarithmic scale allows the ordinate to be considered as a plot of log $(v^{2/5} \cdot Q)$ plus some undetermined constant related to the unknown $n_2 \ell$ product.

B. Experimental Results

1. Differential Cross Sections

Once the experimental data are obtained as detailed in the preceding sections, several different presentations of the data can be made. A semilogarithmic plot of the original data for a typical run (v_r = 1213m/s, Exp. 31Li6) is shown in Figure 3. On this type of plot, undulations appear as shoulders on a decreasing background curve. Since the curve shapes are identical for the curve drawn through the points representing the most probable value of the intensity and a curve drawn through the ends of the ranges, only the

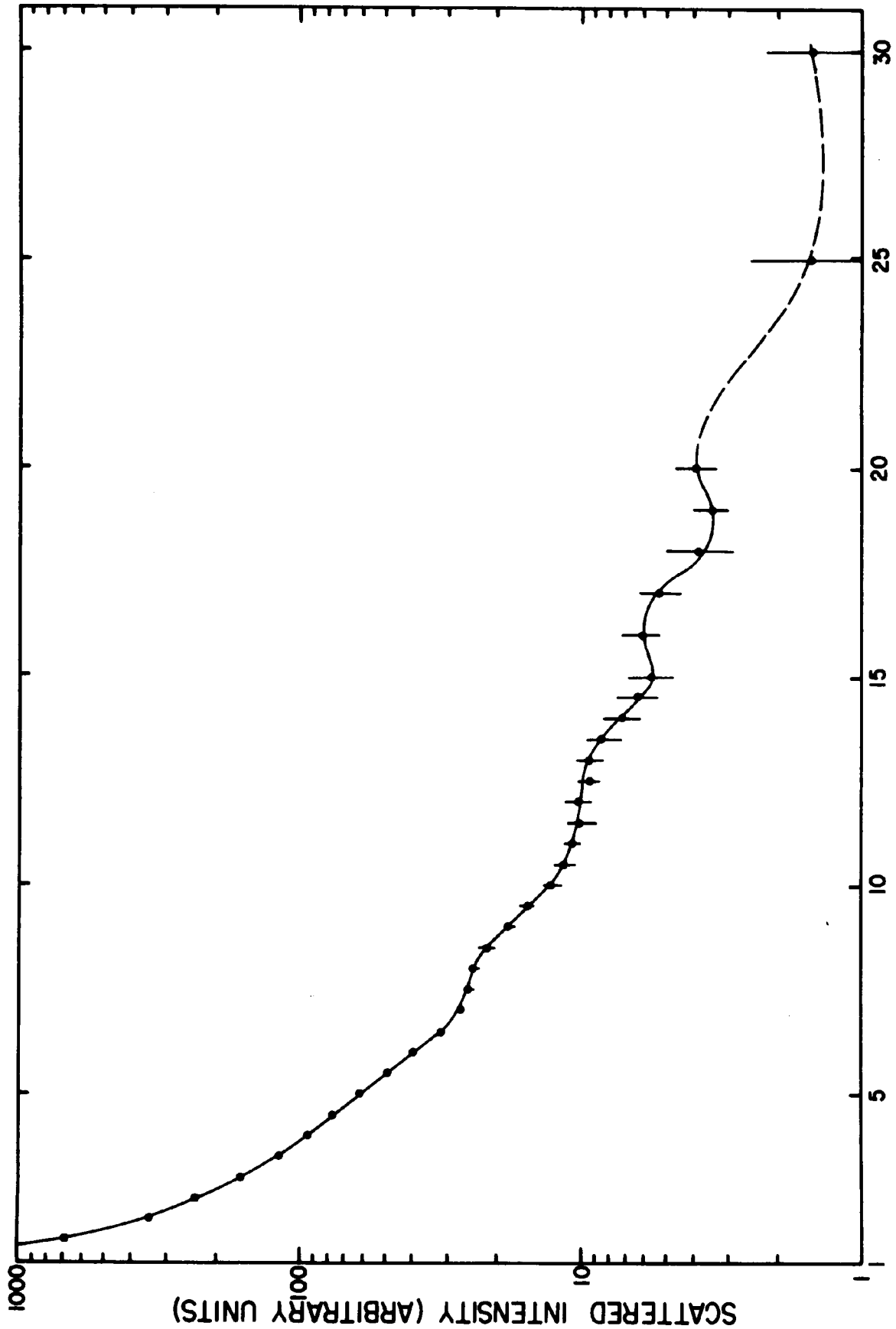


Figure 3. Typical original data: angular distributions; Li^6-Hg, v_r = 1213 m/s

most probable value is used in subsequent calculations. Figure 4 shows this same set of data after conversion to the CM system. Due to the light mass of the Li, the scattering angles are nearly the same in the CM and apparatus systems; in this example, θ_a of 30.0 deg. corresponds to θ of 32.5 degrees. Figure 5 is a log-log plot of the same data. The low angle scattering falls close to the line drawn with the theoretical classical slope of -7/3, suggesting that the $G(\theta)$ presentation might be nearly horizontal. Figure 6 shows the plot of $G(\theta)$ versus θ. This plot is indeed approximately horizontal, with the undulations (Figure 4) now appearing as sinusoidal-like deviations from the smooth curve. Using this type of presentation, the angular positions of the undulations may be located with good sensitivity (e.g. $\pm 0.5^{o}$ for a given experiment).

Angular distribution measurements were performed for beams of Li^6 and Li^7 at several relative velocities. Due to difficulties in maintaining a constant Hg concentration, it is impossible to superimpose replicate runs (i.e. carried out at the same relative velocity) to obtain a unique scattering pattern. If however, the experiments at the same relative velocity are plotted separately on the same angular scale, as in Figures 7 a-c and 8 a-f, then it is possible to estimate the mean positions with uncertainties indicated by the length of the horizontal bars at the bottom of these figures. The numbers (ranging from 1 to 10) associated with the points at the bottom of each graph give a measure of the experimental weights of the various points. High numbers imply a large number of replicate experiments, or that there was exceptionally good agreement between a smaller number of measurements.

Table II and Figure 9 summarize the data. The entries in Table II record the most probable positions of each maximum or minimum; an estimate of the uncertainty in position may be obtained by inspection of Figures 7 and 8. In Figure 9, the pattern of maxima and minima at each value of the relative velocity is plotted at the corresponding

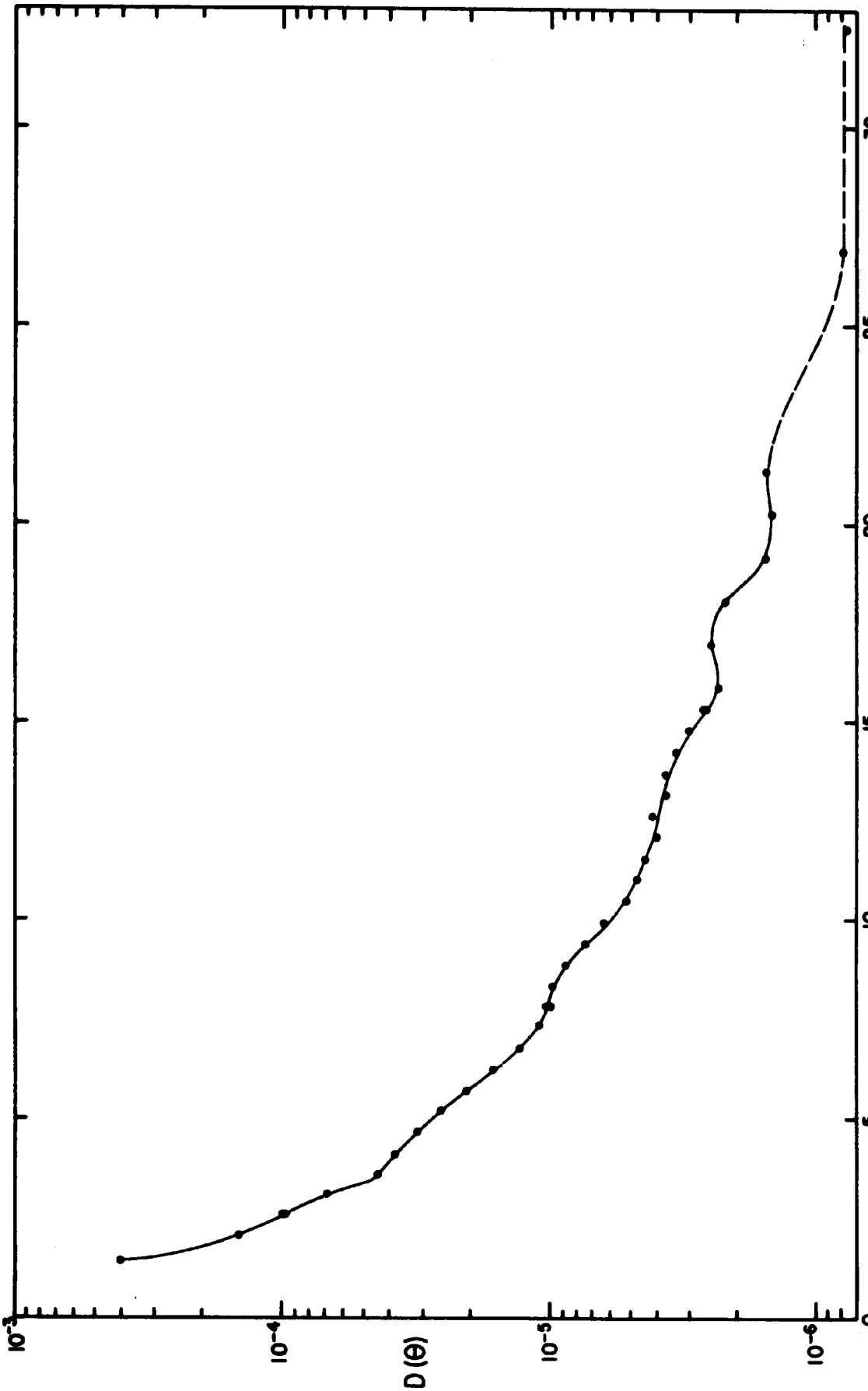


Figure 4. Typical data: center of mass presentation; data of Figure 3

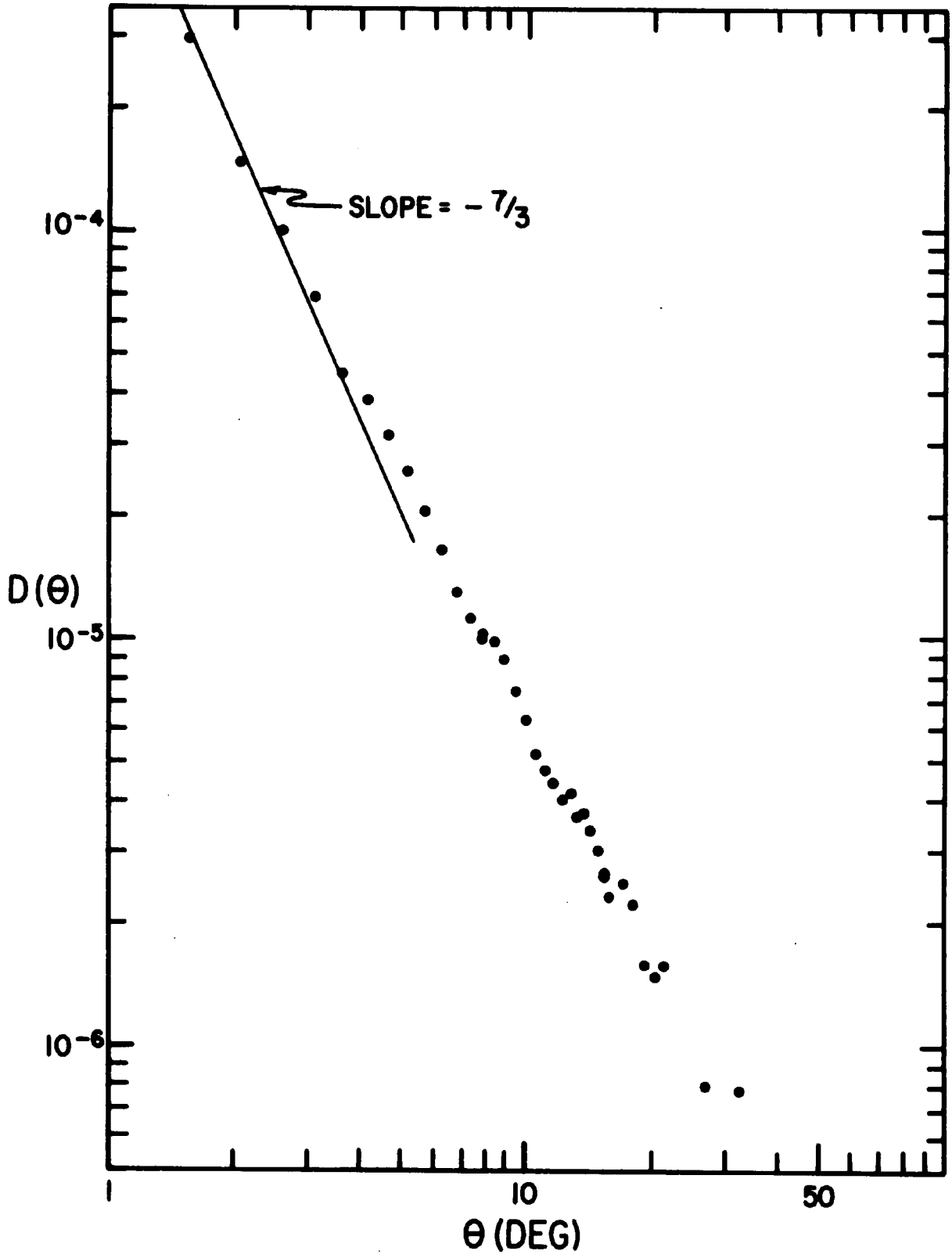


Figure 5. Log-log plot of CM data from Fig. 4

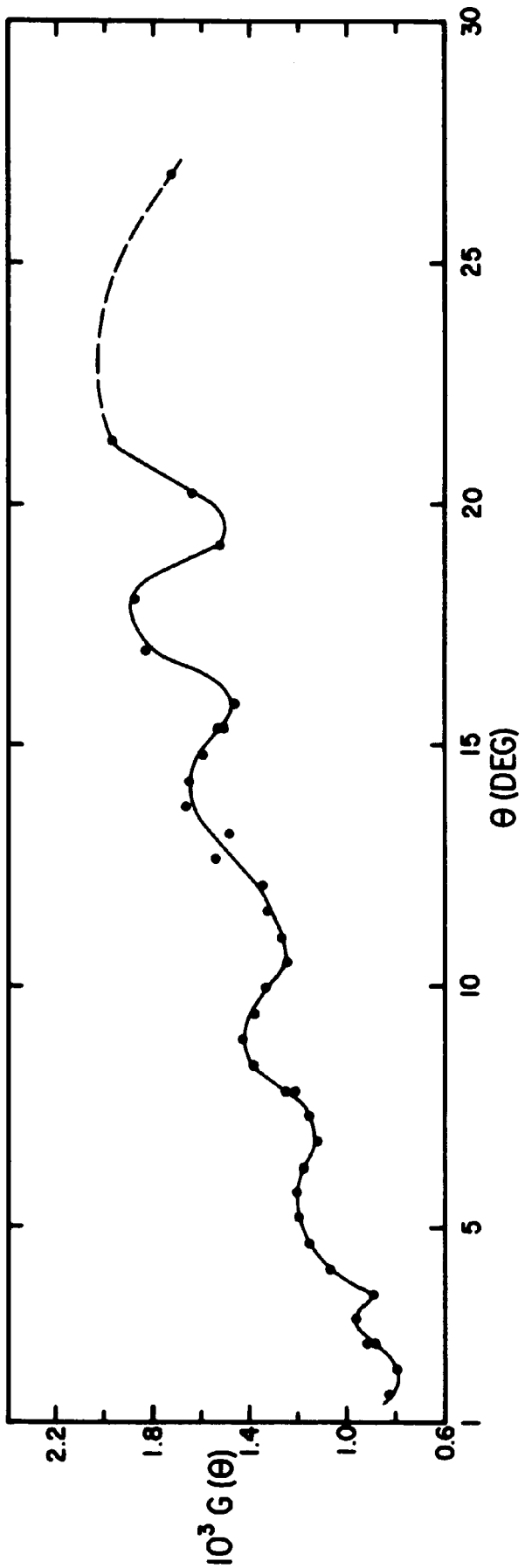


Figure 6. Typical data: G(θ) presentation; same data as Figs. 3-5

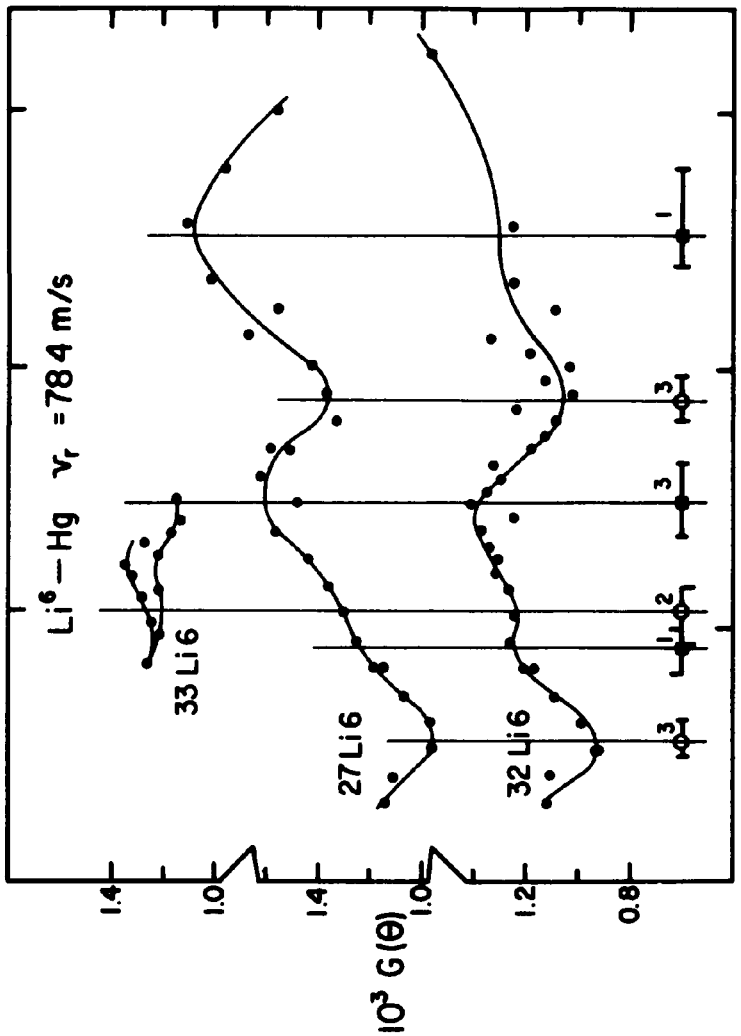


Figure 7a. Experimental data: Li^6-Hg

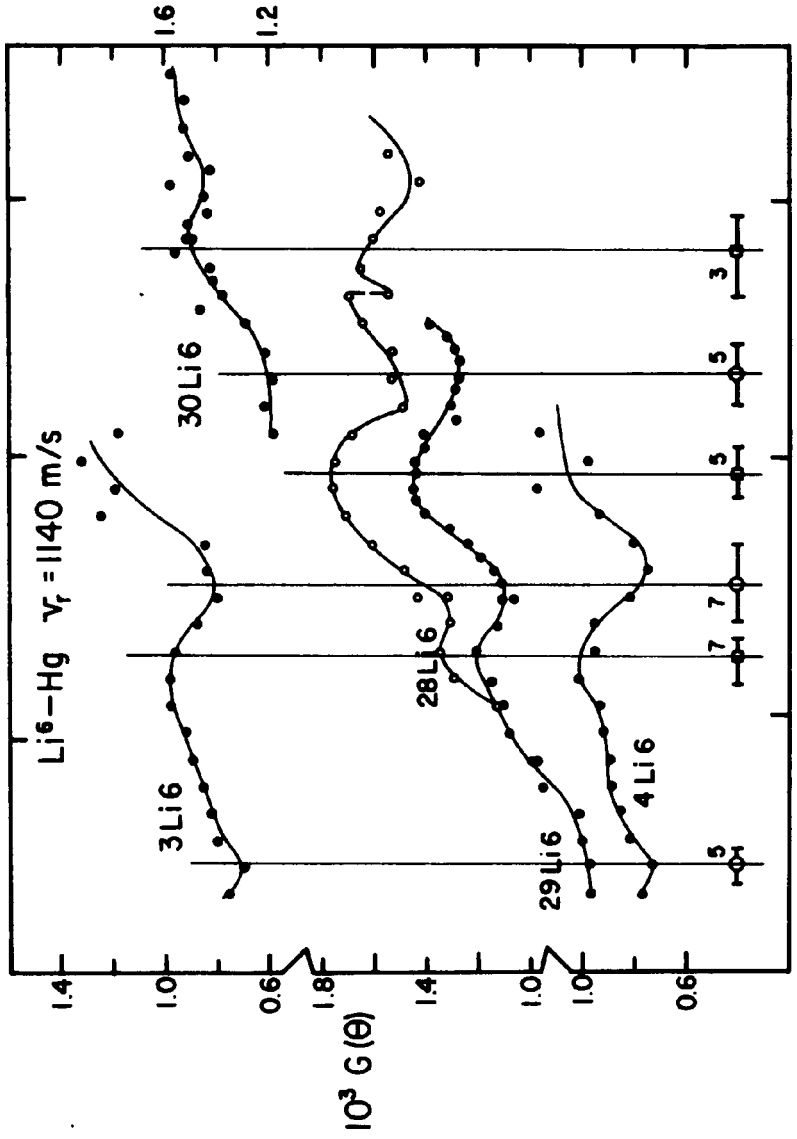


Figure 7b. Experimental data: Li^6-Hg

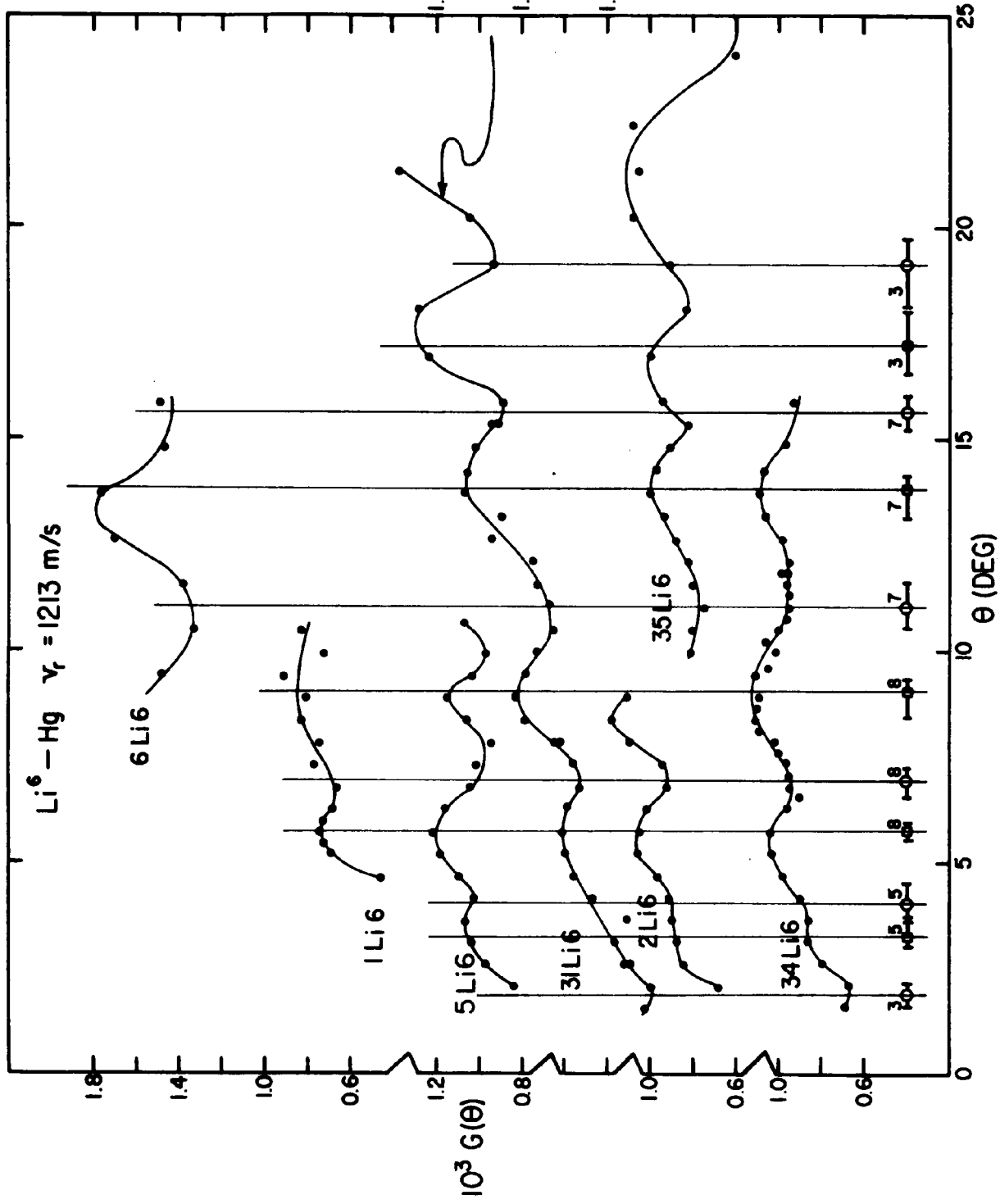


Figure 7c. Experimental data: Li^6-Hg

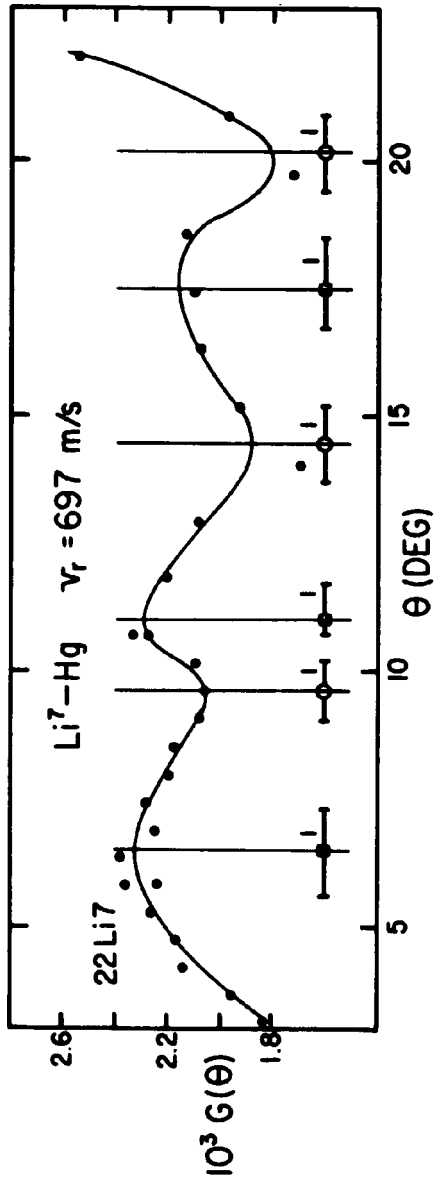


Figure 8a. Experimental data: Li^7-Hg

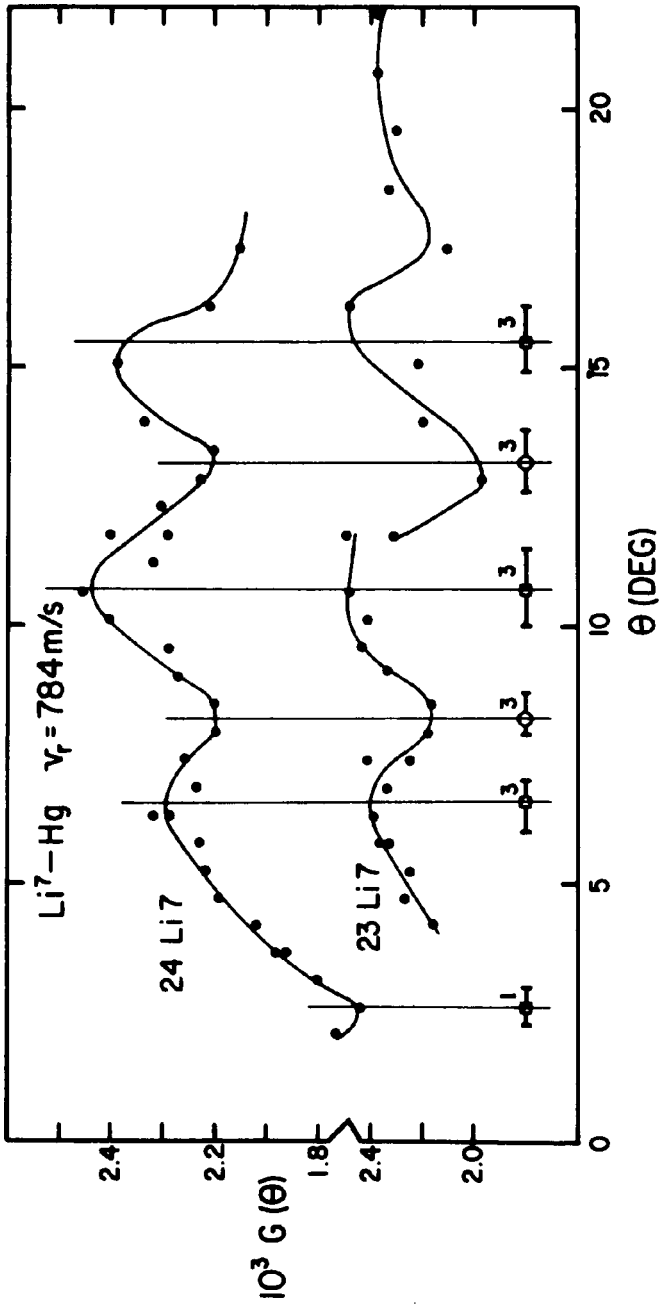


Figure 8b. Experimental data: Li^7-Hg

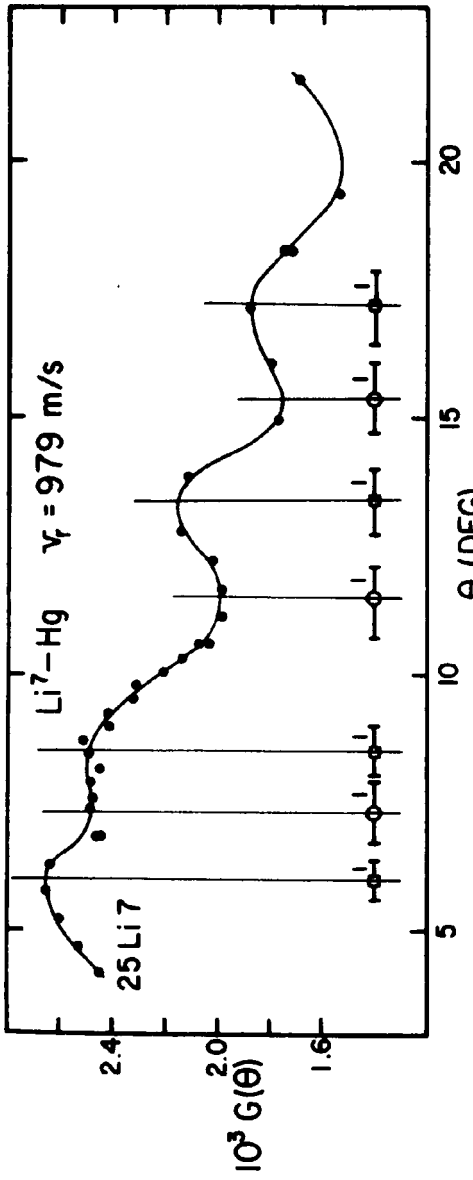


Figure 8c. Experimental data: Li^7-Hg

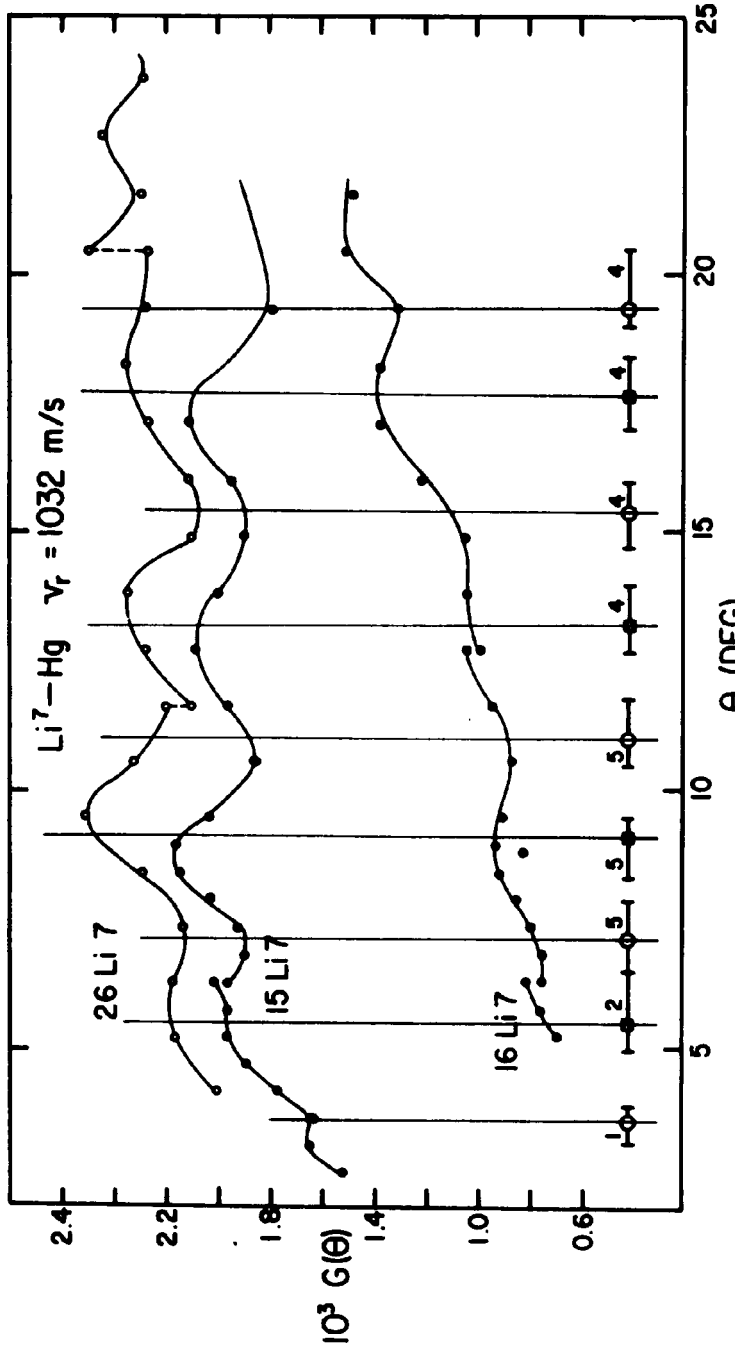


Figure 8d. Experimental data: Li^7-Hg

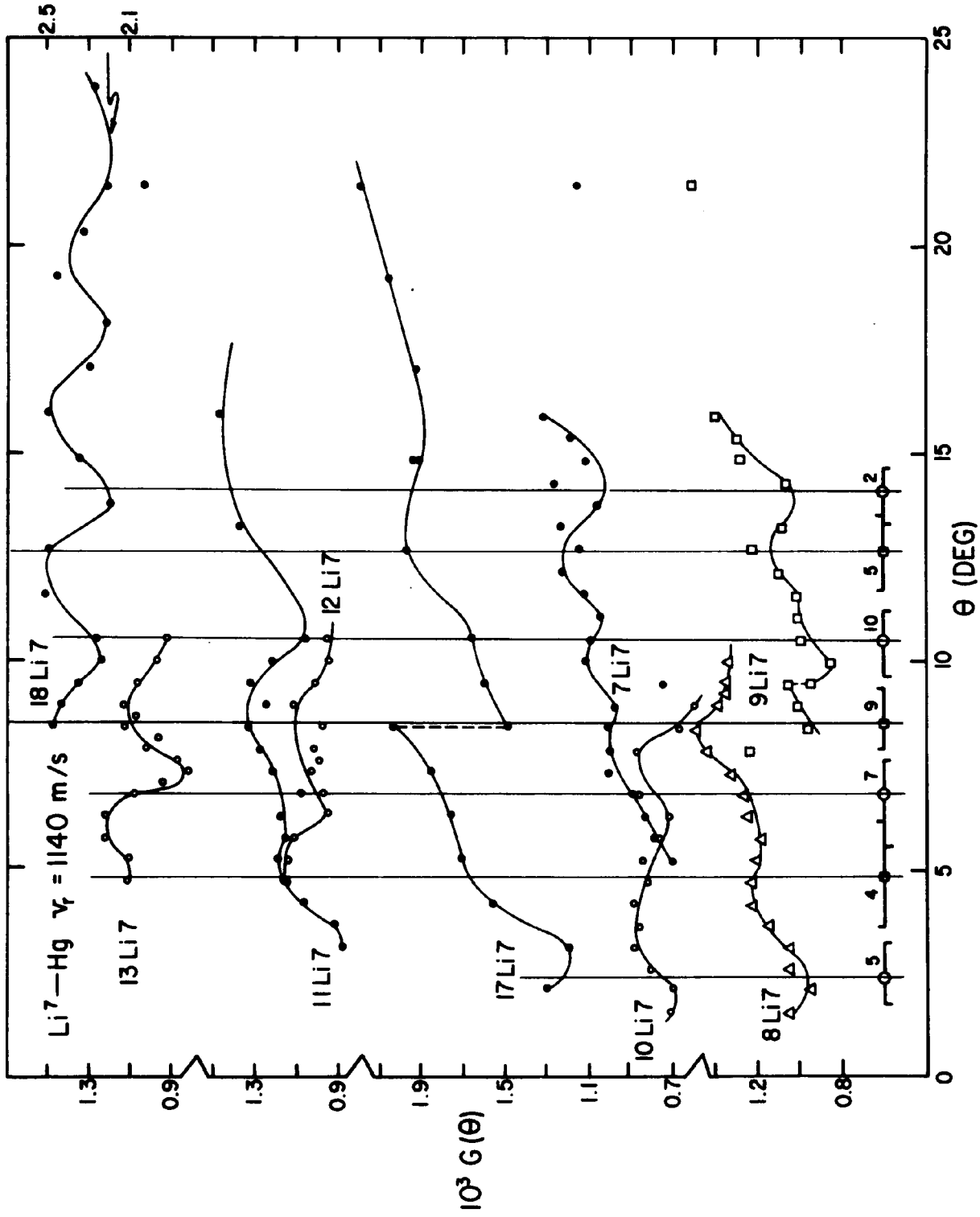


Figure 8e. Experimental data: Li^7-Hg

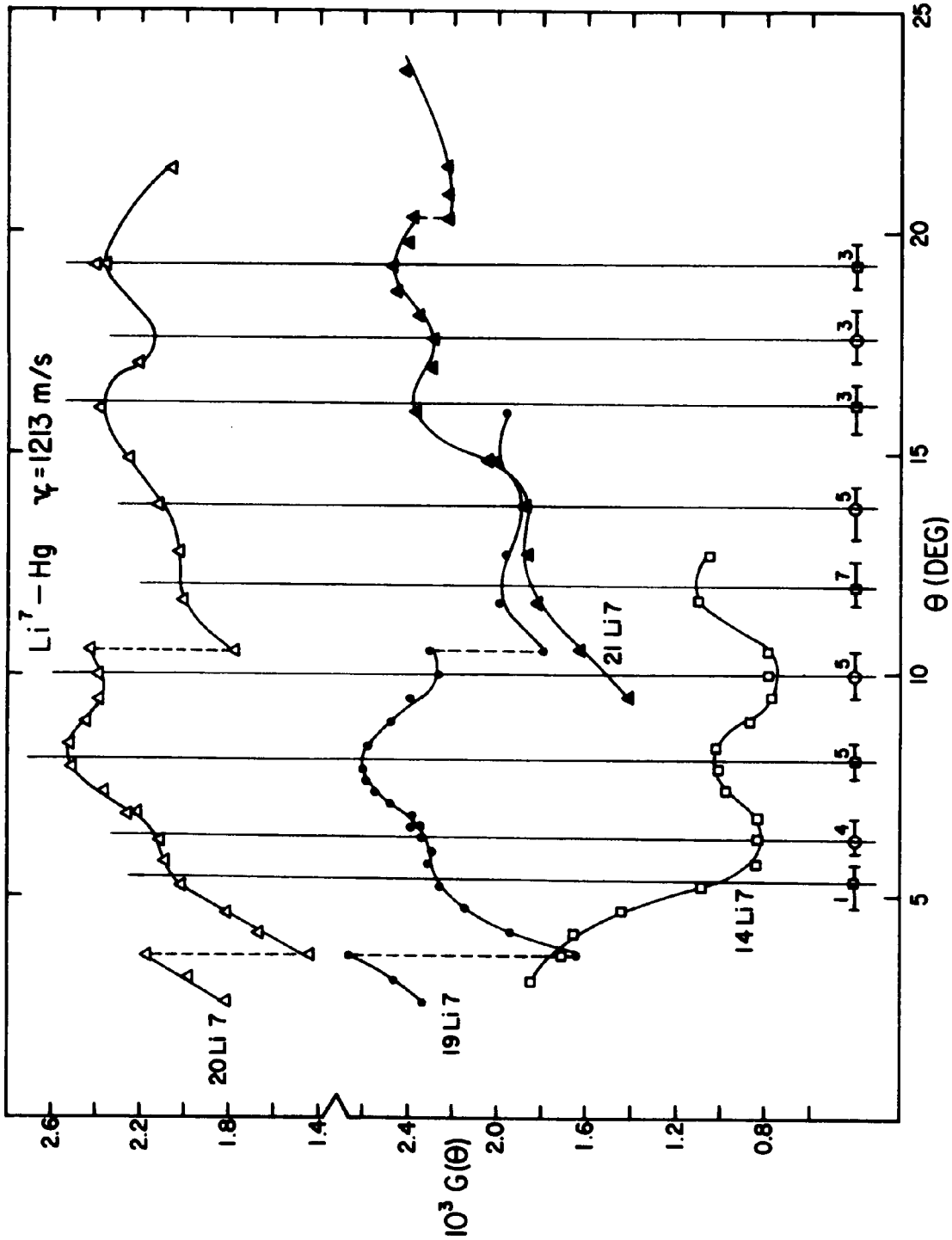


Figure 8f. Experimental data: Li^7-Hg

Table II

Angular Positions of Undulations in Experimental G(θ) Curves

	Li^6			Li^7					
v (m/s)	784	1140	1213	697	784	979	1032	1140	1213
10^{-9}k (cm^{-1})	.721	1.049	1.116	.744	.837	1.045	1.102	1.218	1.295
log k	8.858	9.021	9.048	8.872	8.923	9.019	9.042	9.086	9.112
Min	2.8[a]	2.1	1.8		2.6			2.4	
Max	4.6		3.2						
Min	5.3		4.0				3.6		
Max	7.4	6.1	5.7	6.5	6.6	6.0	5.5	4.8	5.3
Min	9.4	7.5	6.9	9.6	8.2	7.3	7.1	6.8	6.3
Max	12.6	9.7	9.0	11.0	10.7	8.5	9.1	8.5	8.1
Min		11.6	11.0	14.4	13.2	11.5	11.0	10.5	10.0
Max		14.0	13.8	17.5	15.5	13.4	13.2	12.6	12.0
Min			15.6	20.2		15.4	15.4	14.1	13.8
Max			17.2			17.2	17.7		16.1
Min			19.1				19.4		17.6
Max									19.3

- - - - - - - -

[a] Estimates of the uncertainty in these positions are given on figures 7 and 8.

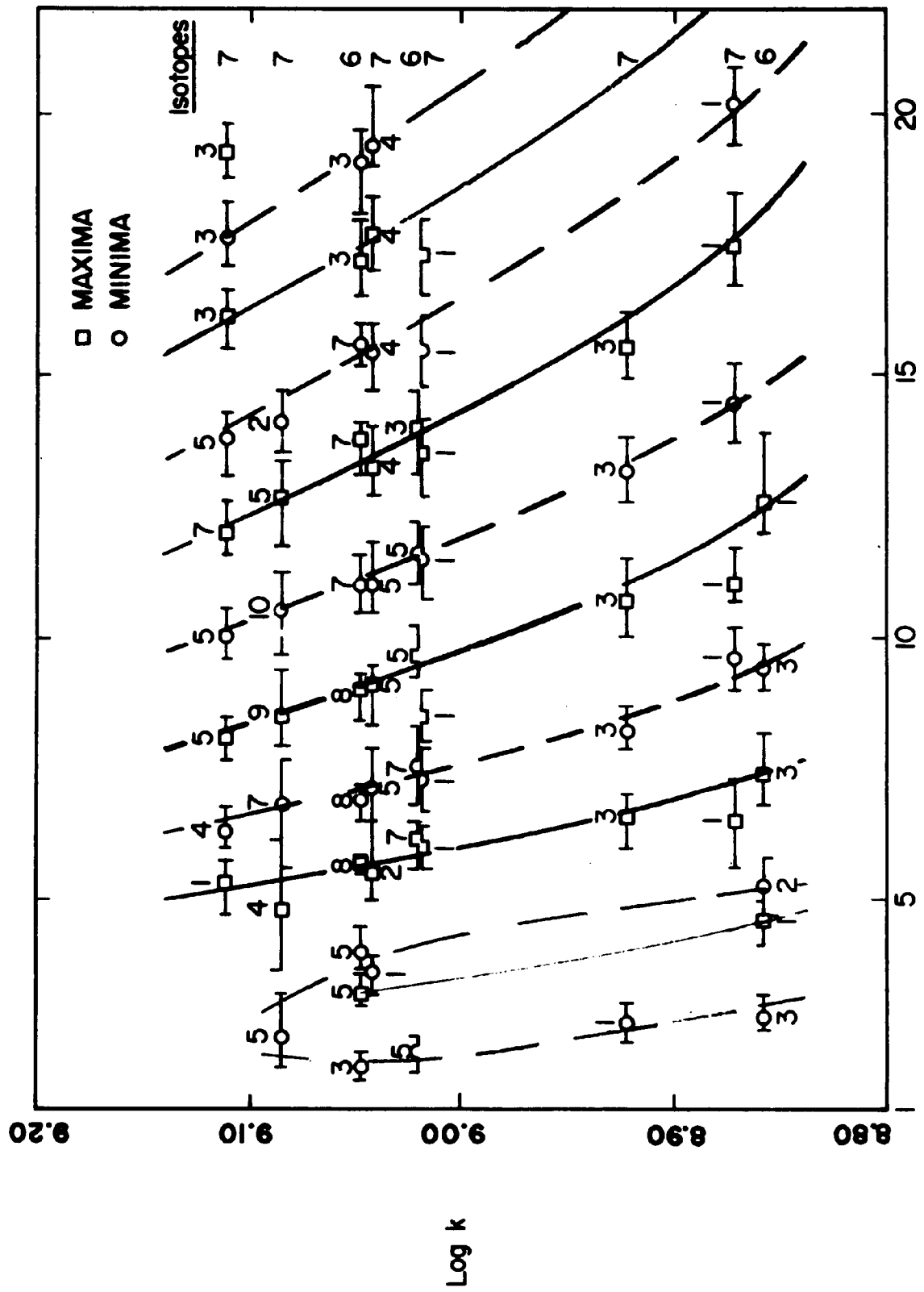


Figure 9. Summary of experimental scattering patterns as a function of the wave number k for Li^6-Hg and Li^7-Hg

value of log k, where the wave number k is given by

$$k = \frac{\mu \bar{v}_L}{\hbar} = \frac{2\pi}{\lambda} \qquad (29)$$

The advantages of this presentation will become apparent later. For the moment, it is sufficient to call attention to the great similarity in the scattering patterns for Li^6 and Li^7 when results at nearly identical values of k are compared.

2. Total Cross Sections

Total cross section measurements were made for both isotopes of Li. As mentioned in section A2, the uncertainty in the Hg concentration prevented the determination of absolute total cross sections, but relative total cross sections were measured.

Figure 10 shows a set of typical original data. Plotted here is I/I_o versus v_{Li}. This type of plot shows some hint of extrema, which are made apparent by Figures 11 and 12, which show the data obtained for Li^6 and Li^7 respectively. The lower sections of these graphs also show predicted patterns of extrema in the total cross sections; these will be discussed later.

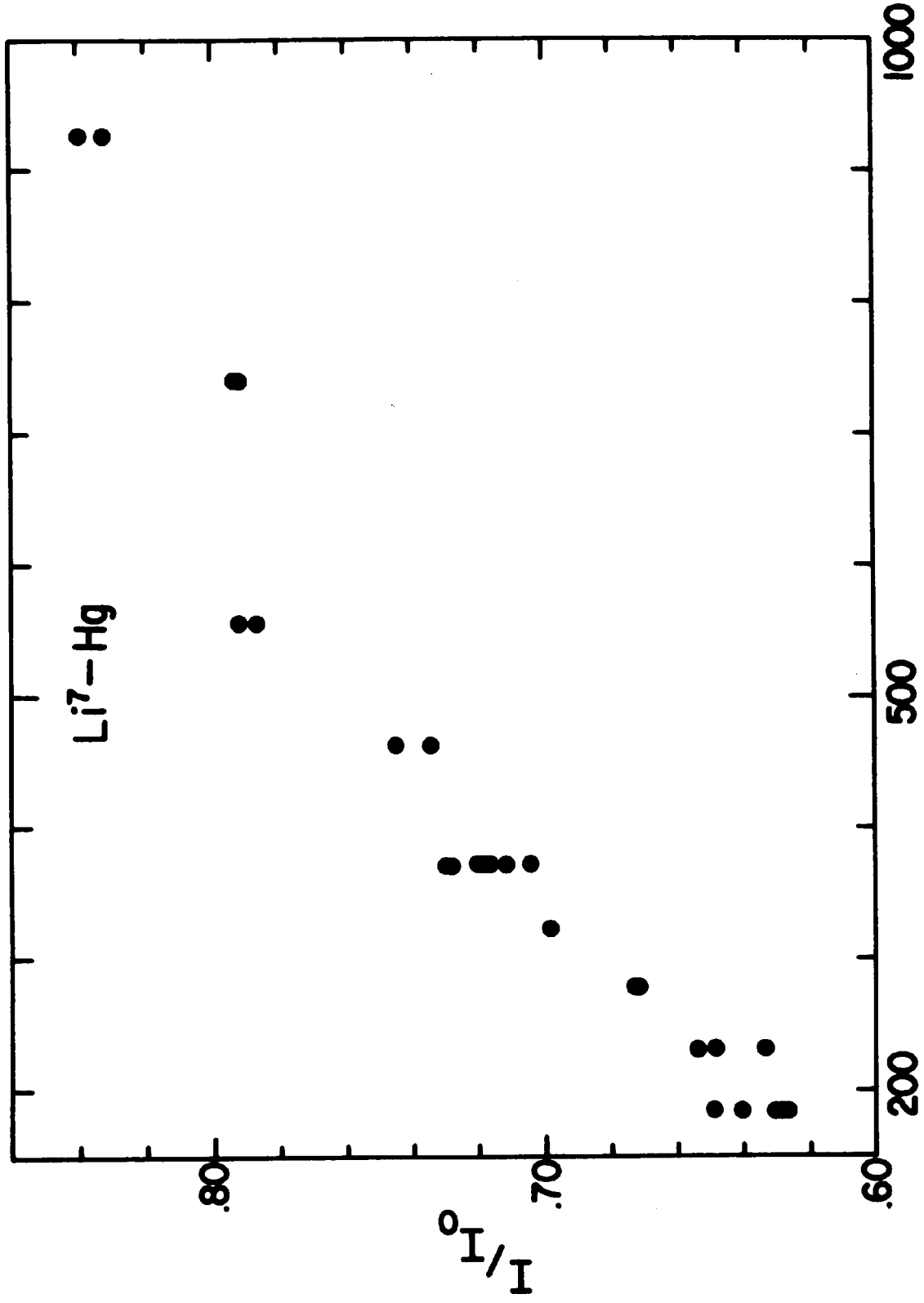


Figure 10. Typical original data on Li beam attenuation, allowing determination of the relative total cross sections

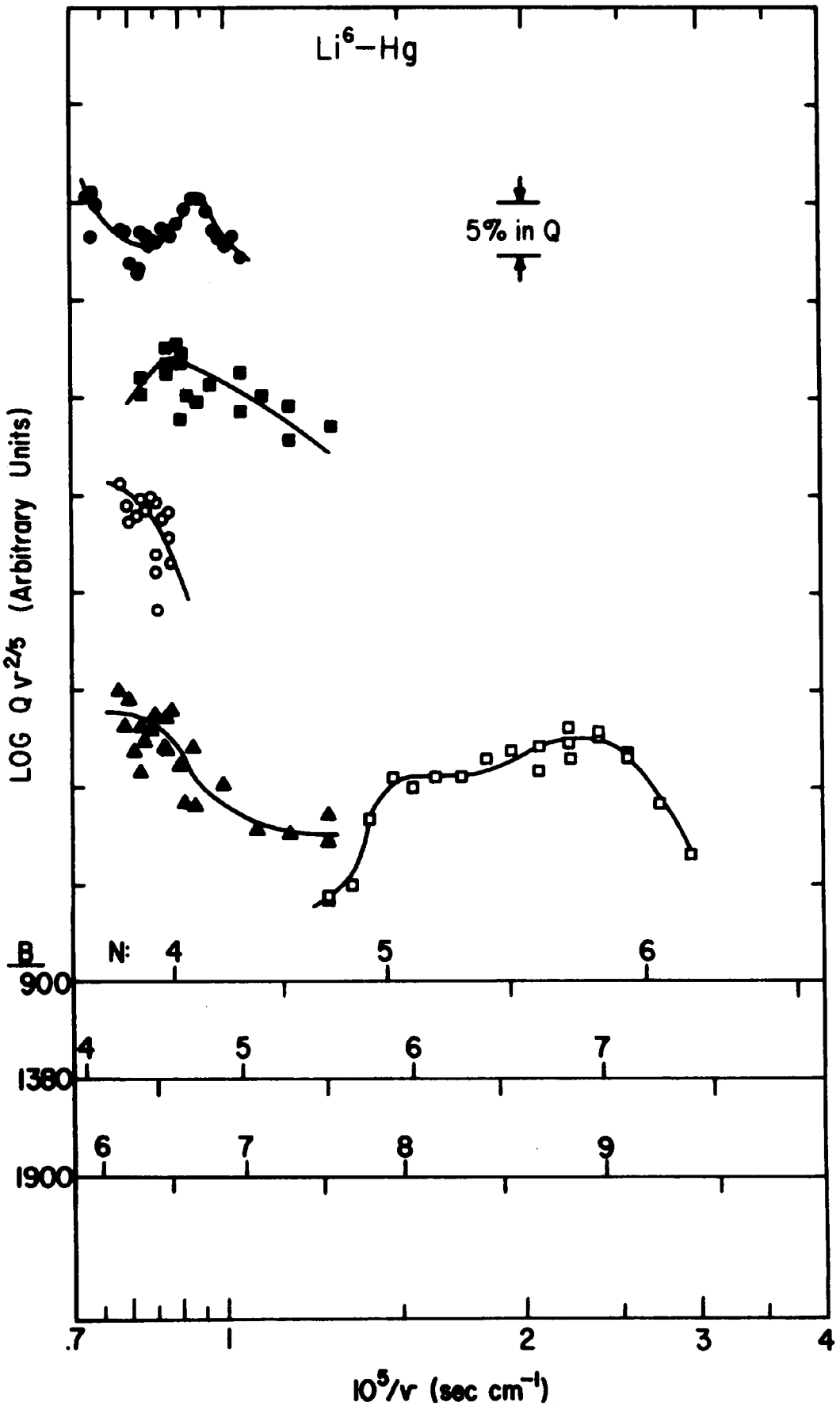


Figure 11. Total cross section data: Li^6. Lower section shows predicted extrema patterns (see Section IV.B.2).

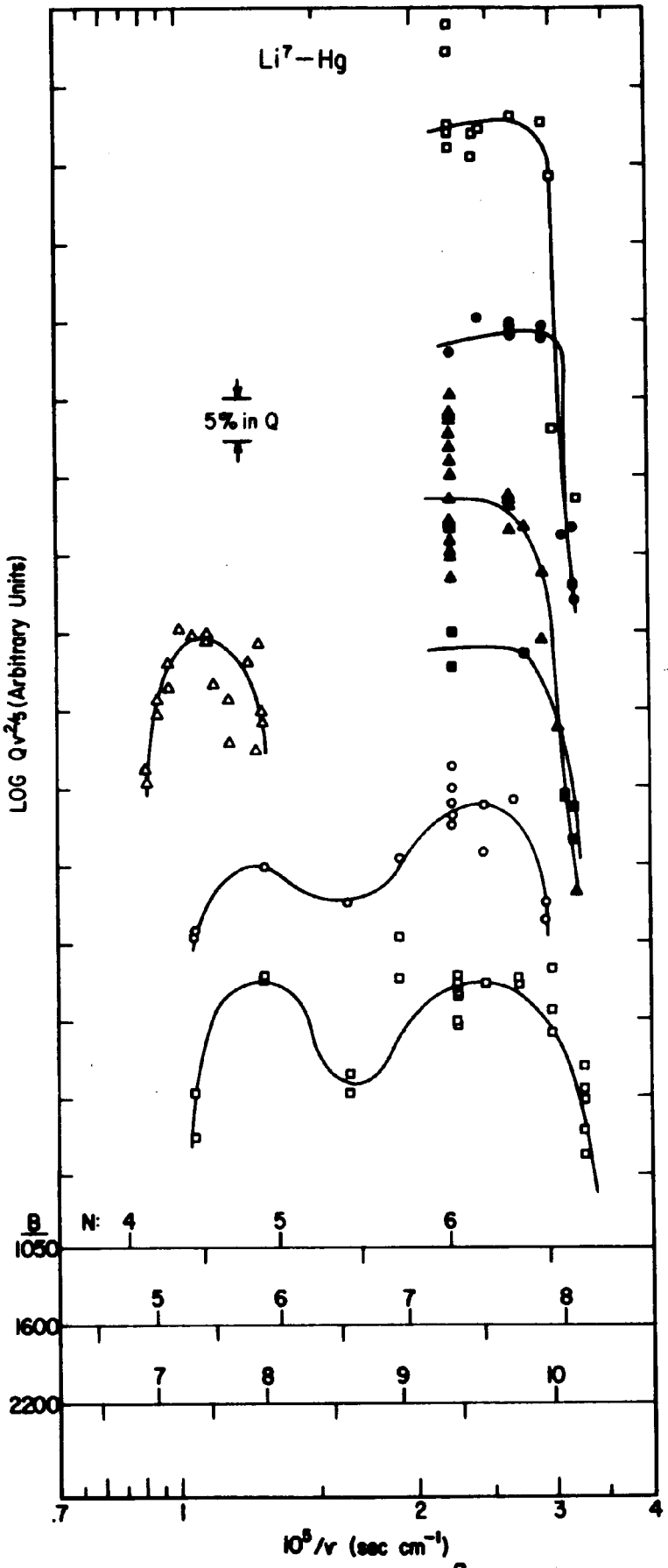


Figure 12. Total cross section data: Li^7. Lower section shows predicted extrema patterns (see Section IV.B.2).

IV. Theoretical Predictions and Comparison with Experimental Results

A. Differential Cross Sections

1. Calculation of Differential Cross Sections

Equation 2 links the set of phase shifts, η_l (k), and the differential cross section I(θ). A dimensionless differential cross section, $I^*(\theta)$, is defined as

$$I^*(\theta) \equiv \frac{I(\theta)}{\pi\sigma^2} \qquad (30)$$

where σ is the L.-J. (12,6) potential parameter assumed. For comparison with the experimental G(θ) curves, analogous theoretical quantities

$$G(\theta) \equiv I(\theta)\ \theta^{\frac{4}{3}}\ \sin\theta \qquad (31a)$$

and

$$G^*(\theta) \equiv I^*(\theta)\ \theta^{\frac{4}{3}}\ \sin\theta \qquad (31b)$$

are defined.

Phase shifts are calculated by numerical solution* (Runge-Kutta-Gill or RKG method) of the one-dimensional radial wave equation, using

- - - - - - - -

* Both the IBM 7090 at the Computing Center of the University of Michigan and the CDC 1604 at the Numerical Analysis Laboratory of the University of Wisconsin have been used for the calculations, with identical results. See appendix A.

the procedure of Bernstein (1960). Briefly, this procedure is: choose $A = k\sigma$ and $B = \frac{2\mu\epsilon\sigma^2}{\hbar^2}$ corresponding to estimated realistic potential parameters for the system of interest. Compute the phase shifts for a number of values of ℓ. Plot these values on a large scale graph of $\eta_\ell(k)$ vs ℓ. Determine the missing values by interpolation. For $\ell \geq 2A$, the Jeffrey's-Born approximation may be used:

$$\eta_\ell(J\text{-}B) = \frac{3\pi}{8} \frac{BA^4}{(\ell+\frac{1}{2})^5} \qquad (32)$$

It is also possible to obtain the set of phase shifts using the reduced phase curves of Bernstein (1960). Phase shifts obtained by this method must be considered only approximate until checks between these phases and the exact phases are carried out. The region on the high ℓ side of the maximum in the phase shift curve is particularly troublesome. Phases from the reduced treatment have been found to differ from the RKG phases by as much as 0.8 rad in this region. Subject to these limitations, the reduced phase treatment is an inexpensive way to obtain the phase shifts. The procedure for these calculations is:

1. Choose A, B, and $K = A^2/B$.
2. Construct a curve of η^* vs β' for the appropriate K, using Table Va of Bernstein (1960).
3. Calculate $\beta' = \frac{\ell+\frac{1}{2}}{A}$ for those ℓ's desired.
4. From the graph of step 2, obtain η^* for each $\beta'(\ell)$.
5. Calculate $\eta = A\eta^*$.

Phase shifts were calculated by these two methods for several values of A at B = 1000, 1500, and 2000. The tables in Appendix A give the values of the phase shifts which were calulated by the exact (RKG) method. The complete set of phase shifts may be obtained from these values by graphical interpolation, or by supplementing these values with values from the reduced phase treatment, or from the Jeffrey's-Born approximation where applicable.

Figure 13 shows a typical calculated angular distribution curve, $I^*(\theta)$, for B = 2000, A = 40; also shown is a semi-log plot of the corresponding $G^*(\theta)$ curve. As mentioned previously, this presentation allows the easy resolution and location of undulations. A typical family of $G^*(\theta)$ curves is shown in Figure 14. In this graph, the ordinate is appropriate for the bottom curve (A = 17.32); each successive curve is displaced vertically by one power of ten. To aid in locating the curves vertically, Table III gives values of $G^*(\theta)$ at the first maximum of each curve. The angular positions of the maxima and minima in the theoretical $G^*(\theta)$ curves are also listed in Table III.

It is particularly interesting to observe the disappearance of the second maximum as A is increased from 27 (B = 1500). When a maximum-minimum pair is just barely detectable as a shoulder on the $G^*(\theta)$ curve, the location is enclosed in parentheses in the table, and a dotted symbol is used in subsequent graphs. Figures 15 a-c display the positions of the maxima and minima as a function of angle. The vertical placement of each horizontal line of points (the scattering pattern) is determined by log A. Lines are then drawn through corresponding undulations. Although each figure corresponds to a different value of B, the curve shapes and the spacing between the undulations is quite similar. Although insensitive to B, the curve shape and spacing depends very strongly upon A. This presentation should allow the prediction of the scattering pattern for any value of A within the range for which the patterns were calculated.

2. Comparison of Theory and Experimental Results

If the experimental scattering patterns can be fitted to the theoretical ones, then the vertical position at which a good fit is

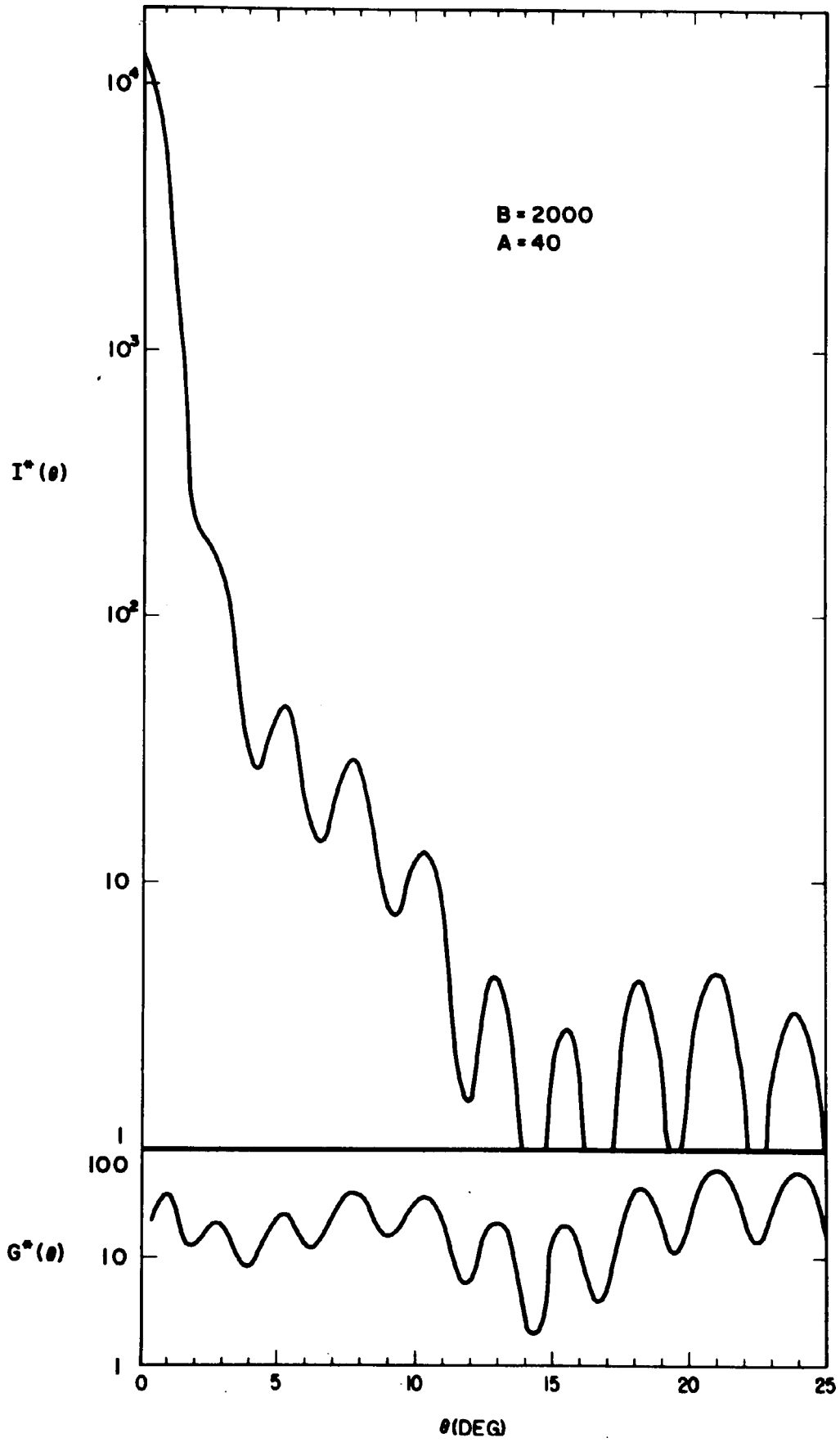


Figure 13. Comparison of $I^*(\theta)$ and $G^*(\theta)$ presentations

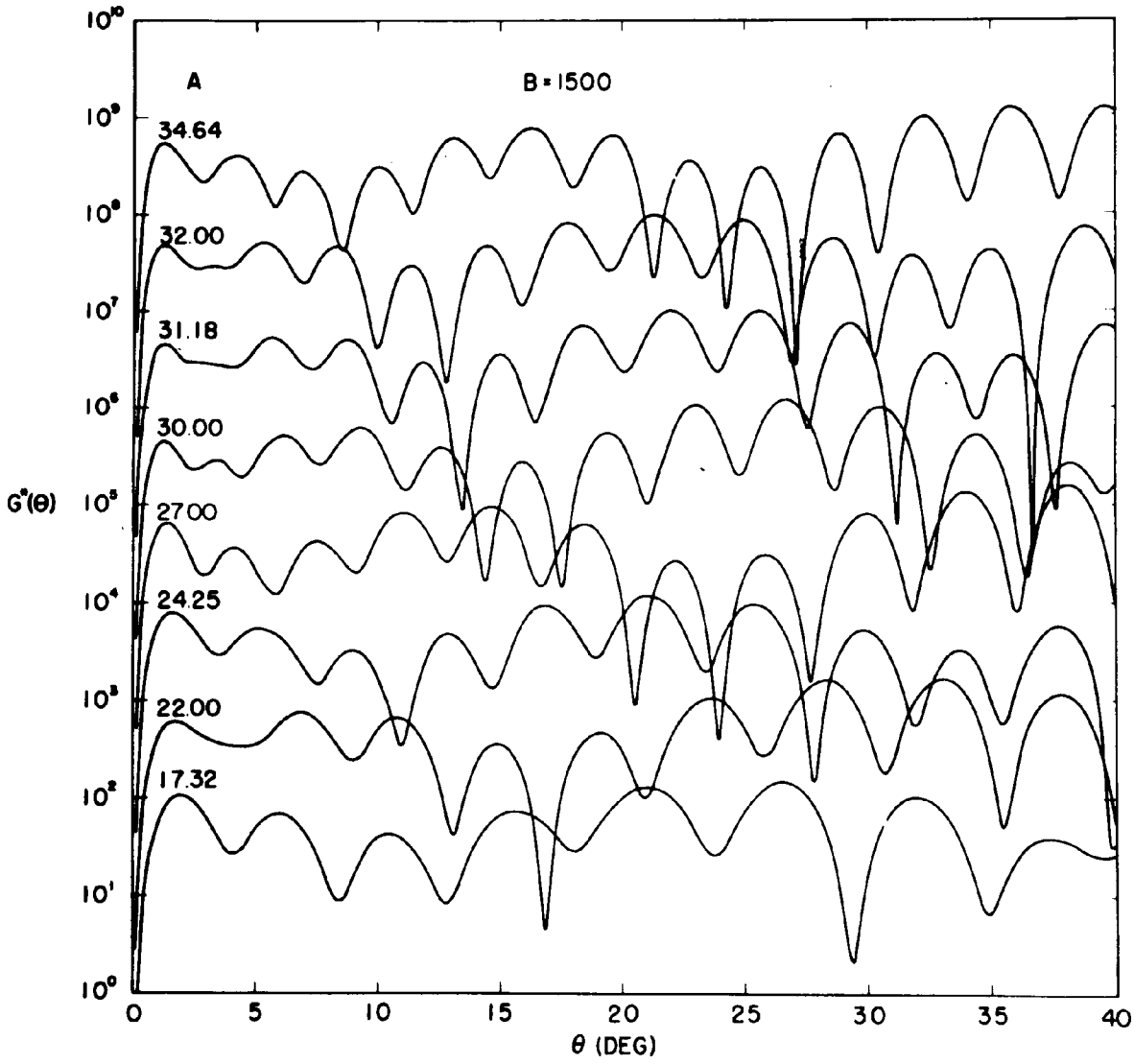


Figure 14. Typical family of G^* (Θ) curves (see Section IV.A.1)

Table IIIa

Angular Positions of Maxima and Minima in Theoretical $G^*(\theta)$ Curves

B = 1000

A	17.32	21.00	28.28	33.64
Q^*	16.80	17.33	14.2	13.87
$G^*(\theta)$ (1st Max.)	65.69	80.00	51.53	54.99
Min	0.0	0.0	0.0	0.0
Max	2.2	1.8	1.5	1.2
Min	5.3	3.9	3.3	2.7
Max	8.7	5.7	5.9	3.8
Min	11.5	8.1	7.9	5.4
Max	13.9	10.0	9.4	7.0
Min	16.9	12.1	11.5	8.3
Max	19.3	14.6	13.1	10.2
Min	21.9	16.7	14.8	11.7
Max	24.4	19.3	16.8	13.5
Min	26.9	21.8	18.5	15.3
Max	29.9	24.4	20.7	17.0
Min	32.7	27.4	22.6	18.9
Max	36.1	29.9	24.7	20.5
Min	39.1		26.9	22.3
Max			29.0	23.8
Min			31.3	25.4
Max			33.4	27.2
Min			35.7	28.9
Max			37.6	30.9
Min			39.4	32.7
Max				34.7
Min				36.6
Max				38.6

Table IIIb

Angular Positions of Maxima and Minima in Theoretical $G^*(\theta)$ Curves

B = 1500

A	17.32	22.00	24.25	27.00	30.00
Q^*	22.15	17.63	19.18	17.17	14.70
$G^*(\theta)$ (1st Max.)	106.79	61.97	80.89	66.90	46.27
Min	0.0	0.0	0.0	0.0	0.0
Max	1.9	1.7	1.6	1.3	1.2
Min	4.1	4.4	3.5	2.8	2.4
Max	5.9	6.8	5.1	4.1	3.3
Min	8.4	8.9	7.5	5.7	4.3
Max	10.4	10.8	8.9	7.4	6.1
Min	12.8	13.0	10.9	9.0	7.5
Max	15.6	14.9	12.8	11.0	9.2
Min	18.0	16.8	14.6	12.8	11.1
Max	21.0	19.1	16.8	14.6	12.5
Min	23.7	20.9	18.9	16.6	14.3
Max	26.5	23.6	21.0	18.4	15.9
Min	29.4	25.8	23.3	20.5	17.5
Max	32.0	28.3	25.4	22.1	19.4
Min	34.9	30.7	27.8	23.9	21.0
Max	37.4	33.1	29.8	25.8	23.0
Min	39.6	35.5	31.9	27.7	24.8
Max		37.8	33.7	30.0	26.7
Min			35.4	31.8	28.7
Max			37.7	34.0	30.5
Min			39.8	36.0	32.6
Max				38.1	34.4
Min					36.4
Max					38.2
Min					39.6

Table IIIc

Angular Positions of Maxima and Minima in Theoretical $G^*(\theta)$ Curves

B = 1500

A	31.18	32.00	34.64	51.96	62.35	83.14
Q^*	14.80	15.09	15.58	13.89	11.36	11.23
$G^*(\theta)$ (1st Max.)	46.50	48.21	55.81	46.61	30.98	33.35
Min	0.0	0.0	0.0	0.0	0.0	0.0
Max	1.2	1.2	1.2	0.85	0.65	0.55
Min	(2.3)	2.6	2.8	1.80	1.40	1.20
Max	(3.0)	3.2	4.2	2.75	1.95	1.70
Min	4.0	3.8	5.7	3.95	2.50	2.50
Max	5.6	5.2	6.8	5.00	3.50	3.15
Min	7.3	6.9	8.5	5.90	4.30	3.85
Max	8.7	8.2	10.0	7.10	5.25	4.70
Min	10.5	9.9	11.4	8.05	6.30	5.35
Max	11.8	11.3	13.1	9.30	7.10	6.20
Min	13.4	12.7	14.6	10.50	8.20	7.00
Max	15.0	14.5	16.3	11.65	9.05	7.75
Min	16.4	15.9	18.0	12.90	10.00	8.60
Max	18.4	17.8	19.6	14.00	11.05	9.35
Min	20.1	19.5	21.3	15.20	11.95	10.15
Max	22.0	21.3	22.8	16.25	13.05	10.90
Min	23.9	23.3	24.3	17.30	14.10	11.60
Max	25.6	25.0	25.7	18.55	15.15	12.50
Min	27.6	27.0	27.1	19.65	16.25	13.25
Max	29.3	28.6	28.9	21.00	17.35	14.15
Min	31.2	30.3	30.5	22.15	18.50	14.95
Max	32.8	31.8	32.3	23.50	19.45	15.85
Min	34.4	33.4	34.1	24.75	20.65	16.70
Max	35.9	35.0	35.9	26.10	21.60	17.60
Min	37.6	36.7	37.8	27.40	22.60	18.50
Max	39.6	38.8	39.6	28.60	23.60	19.40
Min					24.55	20.30
Max					25.70	21.20
Min					26.75	22.15
Max					27.95	23.05
Min					29.00	23.95
Max						24.85
Min						25.85
Max						26.75
Min						27.65
Max						28.55
Min						29.55

Table IIId

Angular Positions of Maxima and Minima in Theoretical $G^*(\theta)$ Curves

B = 2000

A	5.0	10.0	17.0	25.0	30.0
Q^*	30.08	25.05	22.82	19.59	17.55
$G^*(\theta)$ (1st Max.)	119.98	95.77	89.28	69.90	63.56
Min	0.0	0.0	0.0	0.0	0.0
Max	4.7	2.7	1.9	1.4	1.1
Min	7.6	4.6	(3.1)	(2.6)	2.3
Max	10.1	6.0	(4.0)	(3.0)	3.3
Min	14.3	8.7	5.0	3.8	4.7
Max		12.6	8.0	5.6	6.2
Min		15.6	10.2	7.6	7.7
Max		19.1	12.3	9.1	9.3
Min			15.0	11.1	11.2
Max			17.0	12.6	12.7
Min			19.1	14.2	14.6
Max				16.3	16.1
Min				17.9	17.6
Max					19.3

Table IIIe

Angular Positions of Maxima and Minima in Theoretical $G^*(\theta)$ Curves

B = 2000

A	40.0	47.58	60.0	80.0
Q^*	16.35	14.64	13.01	12.31
$G^*(\theta)$ (1st Max.)	56.85	42.21	36.02	34.38
Min	0.0	0.0	0.0	0.0
Max	0.9	0.85	0.65	0.55
Min	2.0	1.85	1.35	1.15
Max	2.8	(2.2)	1.90	1.60
Min	3.9	(2.5)	2.50	2.20
Max	5.3	3.50	3.50	2.95
Min	6.3	4.75	4.30	3.65
Max	7.8	5.65	5.20	4.40
Min	9.1	6.85	6.35	5.15
Max	10.3	7.95	7.05	5.90
Min	11.8	8.90	8.10	6.75
Max	13.0	10.20	9.05	7.40
Min	14.3	11.30	9.85	8.20
Max	15.5	12.50	10.95	8.95
Min	16.8	13.75	11.85	9.65
Max	18.2	14.95	12.90	10.55
Min	19.6	16.30	13.95	11.25
Max	21.1	17.40	15.00	12.15
Min	22.5	18.75	16.10	13.00
Max	24.0	19.80	17.05	13.85
Min	25.6	20.85	18.20	14.75
Max	27.0	22.15	19.15	15.55
Min	28.5	23.25	20.15	16.45
Max	29.8	24.65	21.15	17.25
Min		25.90	22.10	18.10
Max		27.30	23.25	18.90
Min		28.65	24.25	19.65
Max		29.95	25.45	20.50
Min			26.50	21.25
Max			27.65	22.20
Min			28.80	23.00
Max			29.95	23.95
Min				24.80
Max				25.75
Min				26.65
Max				27.55
Min				28.45
Max				29.40

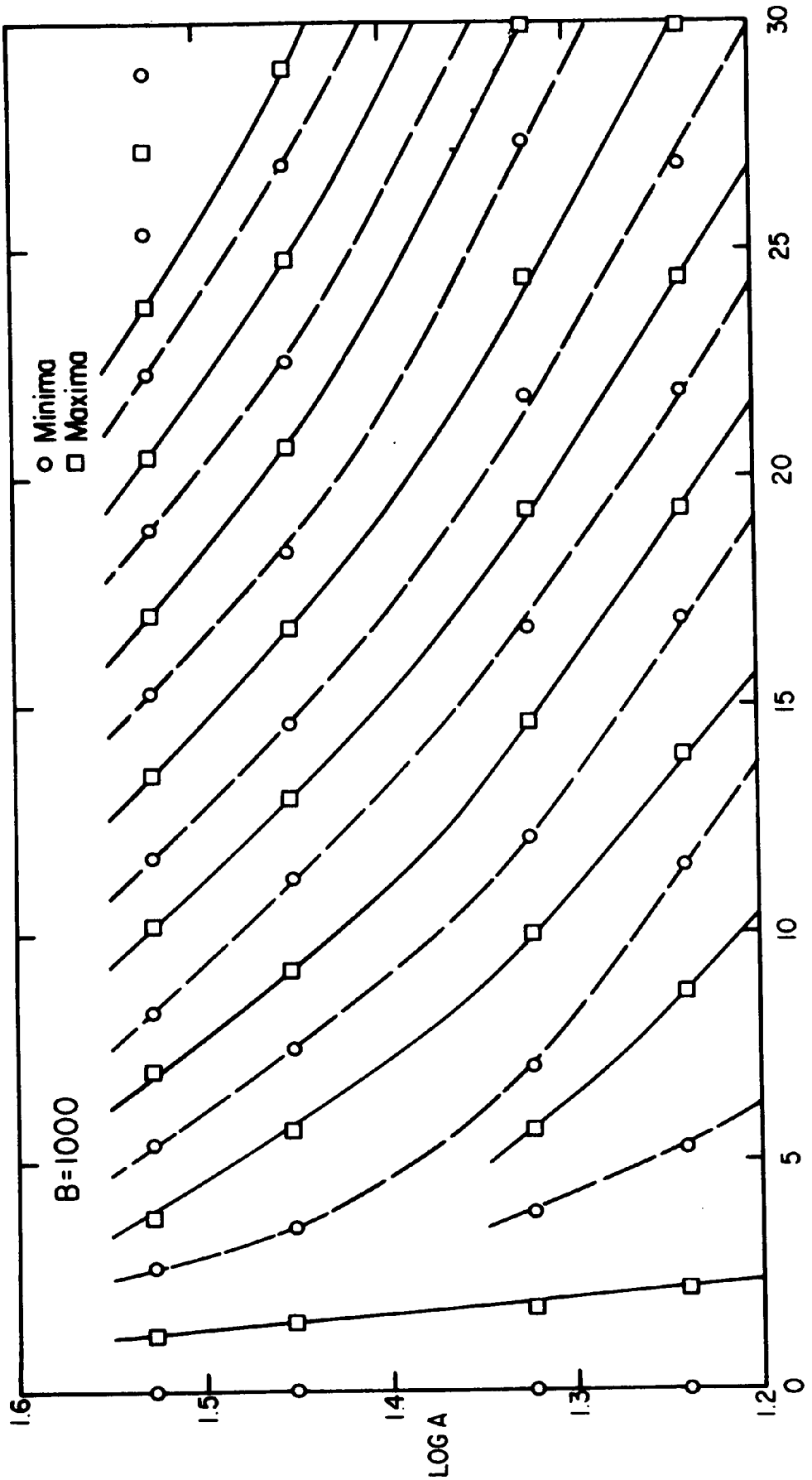


Figure 15a. Scattering patterns: B = 1000

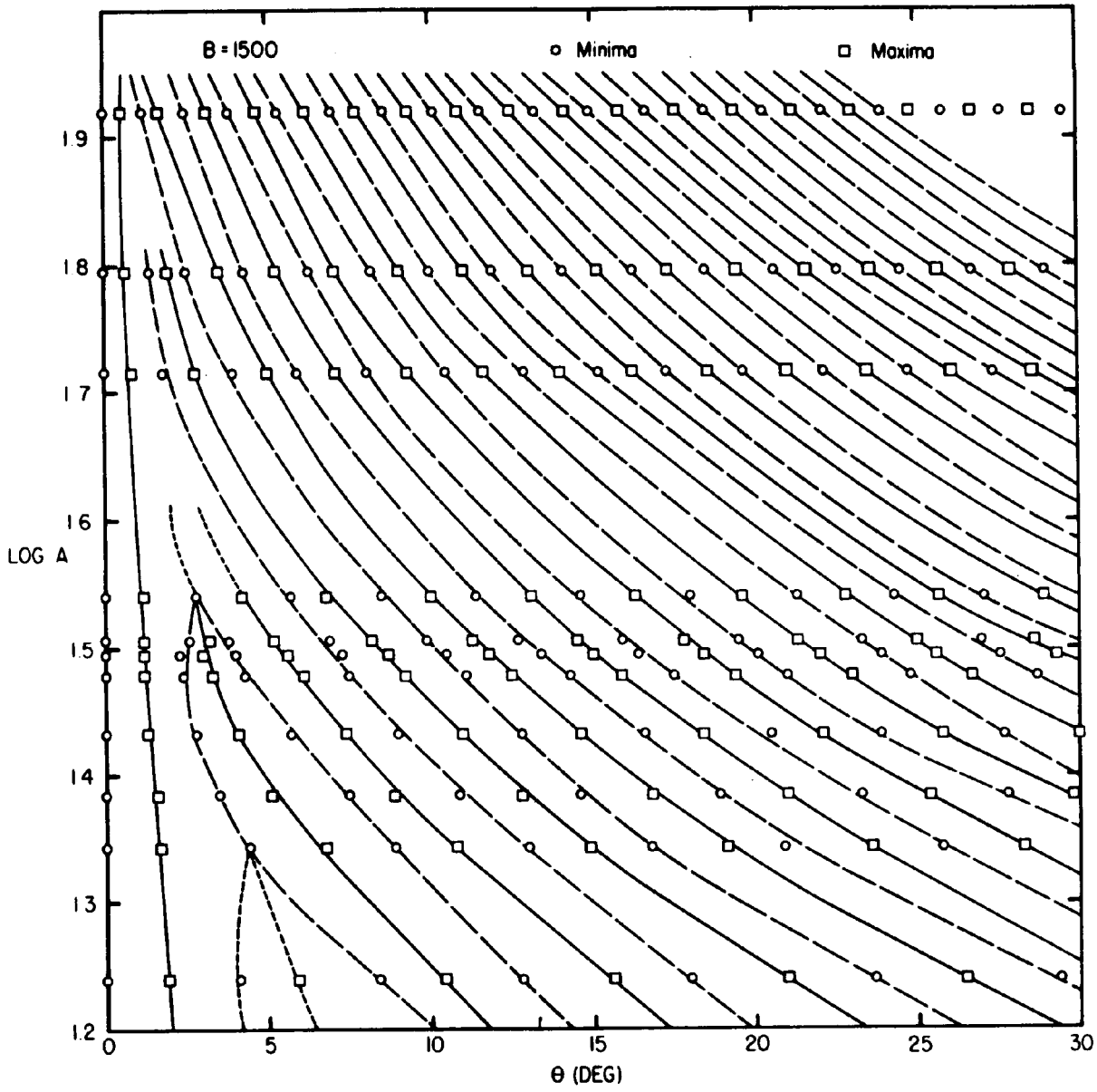


Figure 15b. Scattering patterns: B = 1500

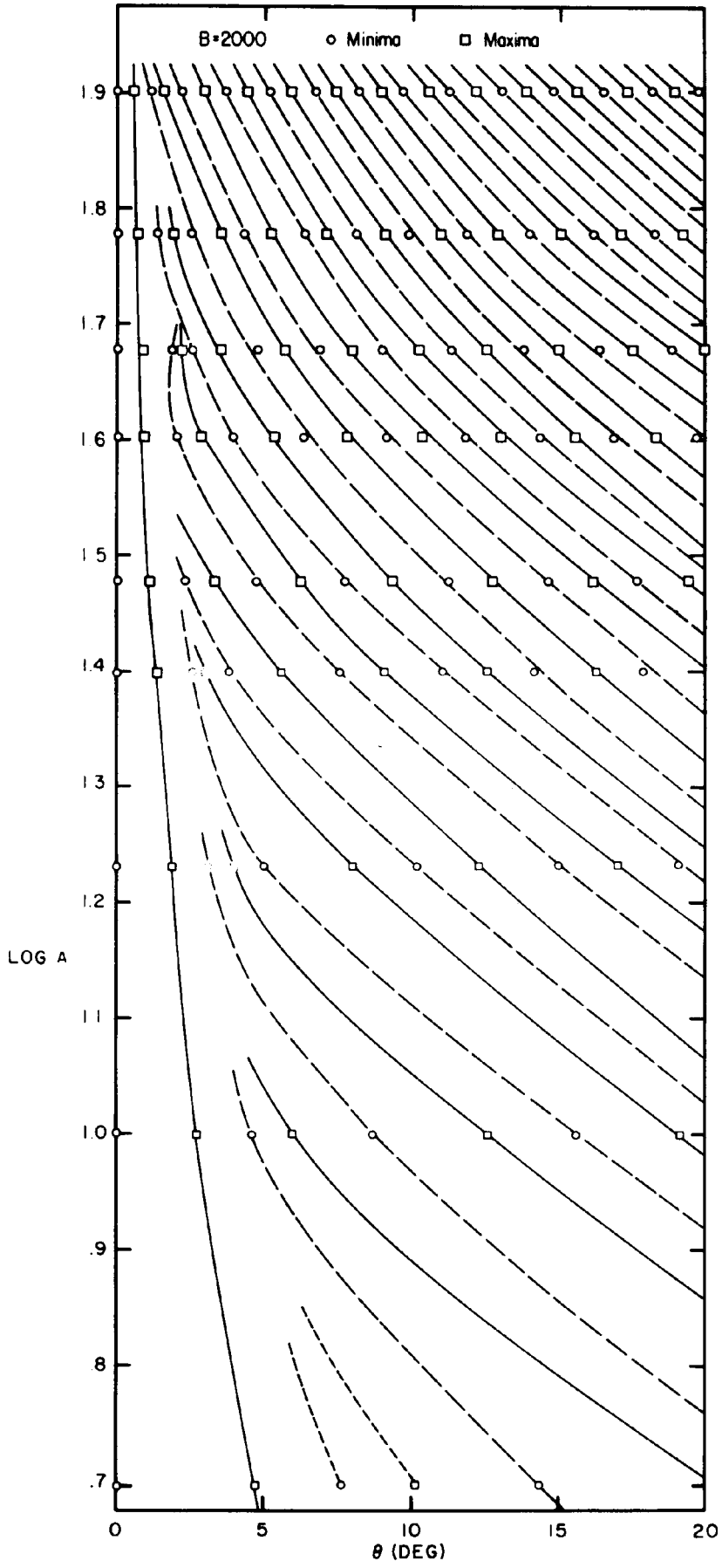


Figure 15c. Scattering patterns: B = 2000

obtained should determine σ directly. The set of experimental points* shown in Figure 9 was superimposed upon each theoretical scattering pattern curve at a number of positions corresponding to values of σ ranging from 2Å to 6Å. Figures 16 a-c show the superpositions of the experimental data on the theoretical curves at which the best agreement between theory and experiment was found. The maximum possible sum of the weights of the experimental points is 250; for the best fits, only about 160/250 of the total weight of the points agrees with theory. Table IV lists the values of σ obtained by this superposition procedure. From the values of σ and B, it is possible to calculate a value for ϵ (using μ for Li^7); these values of ϵ are also shown in Table IV.

Table IV

Potential Parameters Determined From Angular Distributions

	(1)	(2)	(3)
B(nominal)	1000	1500	2000
σ (Å)	2.52	3.47	2.80
$10^{14}\epsilon_{(erg)}$	7.8	6.2	12.6

The fits between the experimental data and the theoretical predictions must be regarded as compromises. If the data are fitted at high A, where the slope of the theoretical curves is as steep as the slope of the experimental curves, then the spacing between adjacent undulations is wrong. If, on the other hand, the spacing is fitted, then the slopes are wrong. The fits shown are compromises between these two problems; the spacings were fitted, while trying to get as nearly the correct slope as possible. Of the three, both the slope and

- - - - - - - -

* No attempt to fit the experimental points for each isotope separately was made. The experimental points for both isotopes agreed well, and the theoretical curves appear to be insensitive enough to B so that the 14% difference in B due to the different reduced masses should not affect the results.

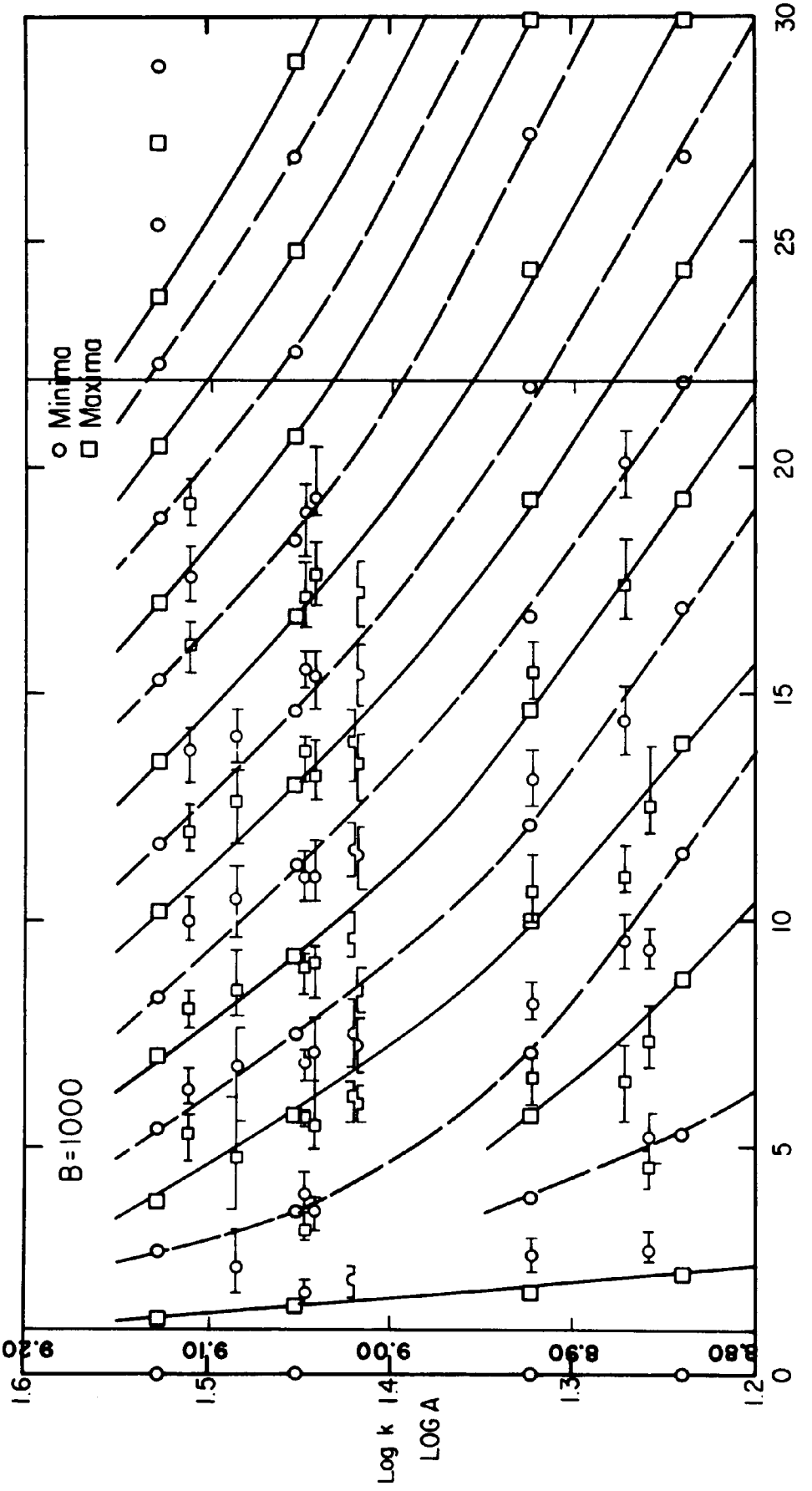


Figure 16a. Comparison of theoretical and experimental scattering patterns: B = 1000

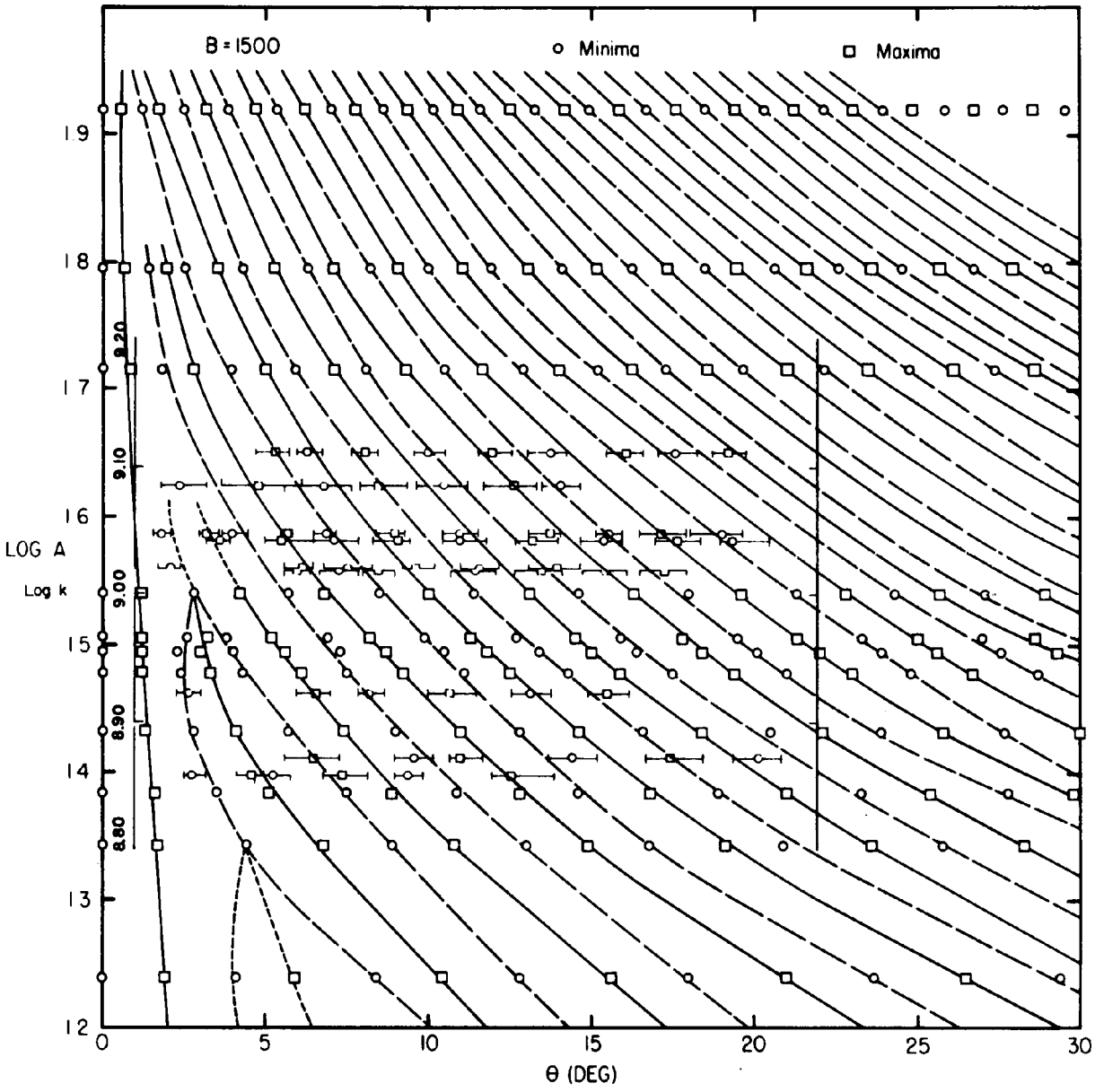


Figure 16b. Comparison of theoretical and experimental scattering patterns: B = 1500

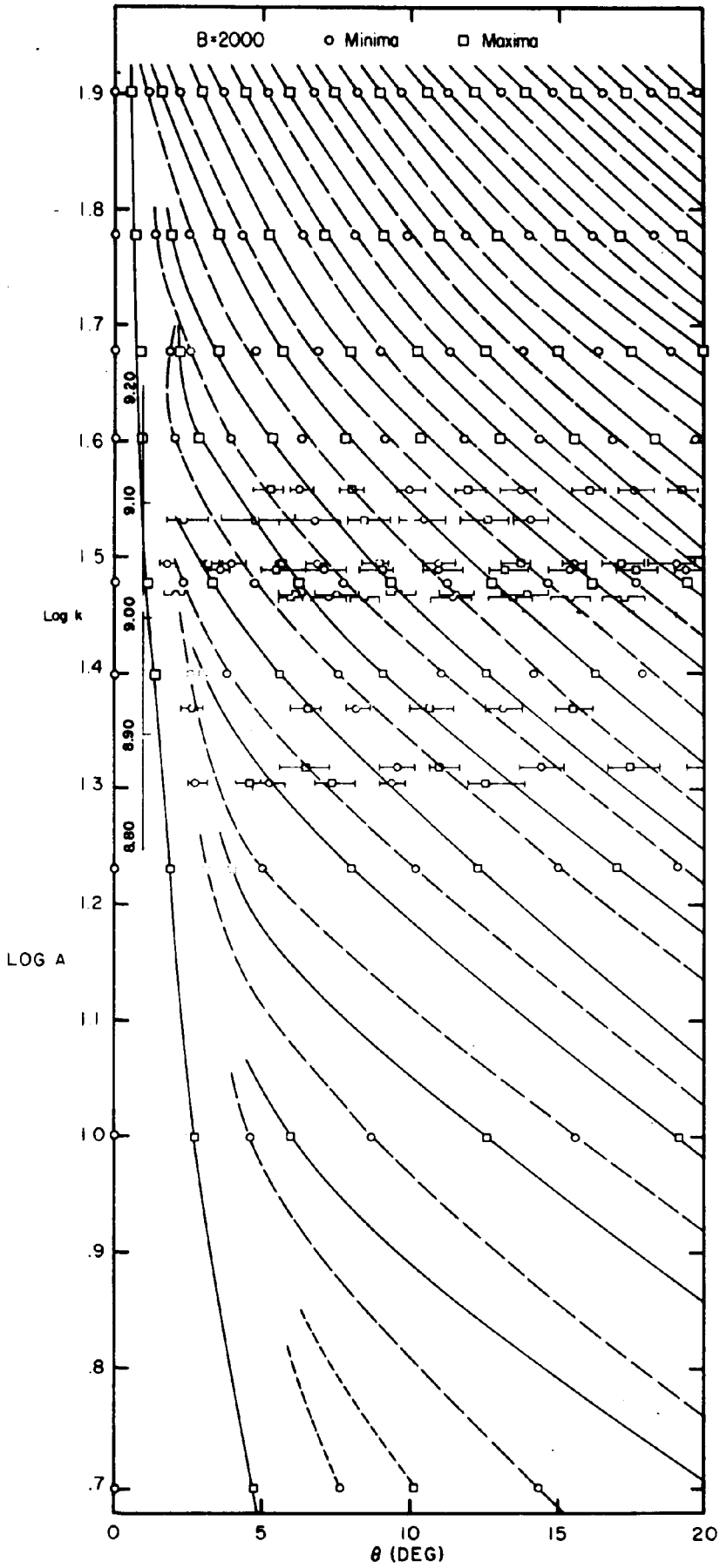


Figure 16c. Comparison of theoretical and experimental scattering patterns: B = 2000

the spacing are most nearly correct when the experimental points are compared with the curves calculated for B = 1000 (Set 1).

B. Total Cross Sections

1. Calculation of Total Cross Sections

Equation 1 allows the calculation of total cross sections from a set of phase shifts. When large numbers of cross sections, Q, over a wide range of relative velocities are required, as, for example, in the prediction of extrema patterns in the atom-atom impact spectrum, the phase shift computations become time-consuming and costly. To circumvent this, one may employ a semiclassical procedure based upon the L.-J. (12,6) potential (Bernstein, 1963) which predicts quite accurately the location of these extrema.

In this procedure, the extrema are assigned index numbers N; the maximum deviation from smooth Massey-Mohr behavior occuring at highest velocity is assigned N = 1, the next minimum is N = 1.5, and so on in order. A reduced velocity parameter

$$D \equiv \frac{B}{A} = \frac{2\epsilon\sigma}{\hbar v} \qquad (33)$$

is defined. In terms of this parameter, the quantity y is obtained from

$$y = 0.1506\, D \left(1 - 0.25\, D \cdot B^{-\frac{1}{2}}\right) . \qquad (34)$$

The values of D for which y becomes equal to N - 3/8 (at a given value of B) are designated D_N; from these D_N, the velocities, v_N, at which the extrema occur can be obtained if given an assumed set of potential parameters. Alternatively, if experimental extrema velocities are available, the potential parameters can be estimated. Figure 5 of Bernstein (1963) shows the behavior of the extrema as a function of D for several B. In order to allow the prediction of extrema patterns for any B, an interpolation graph, Figure 17, was constructed. The

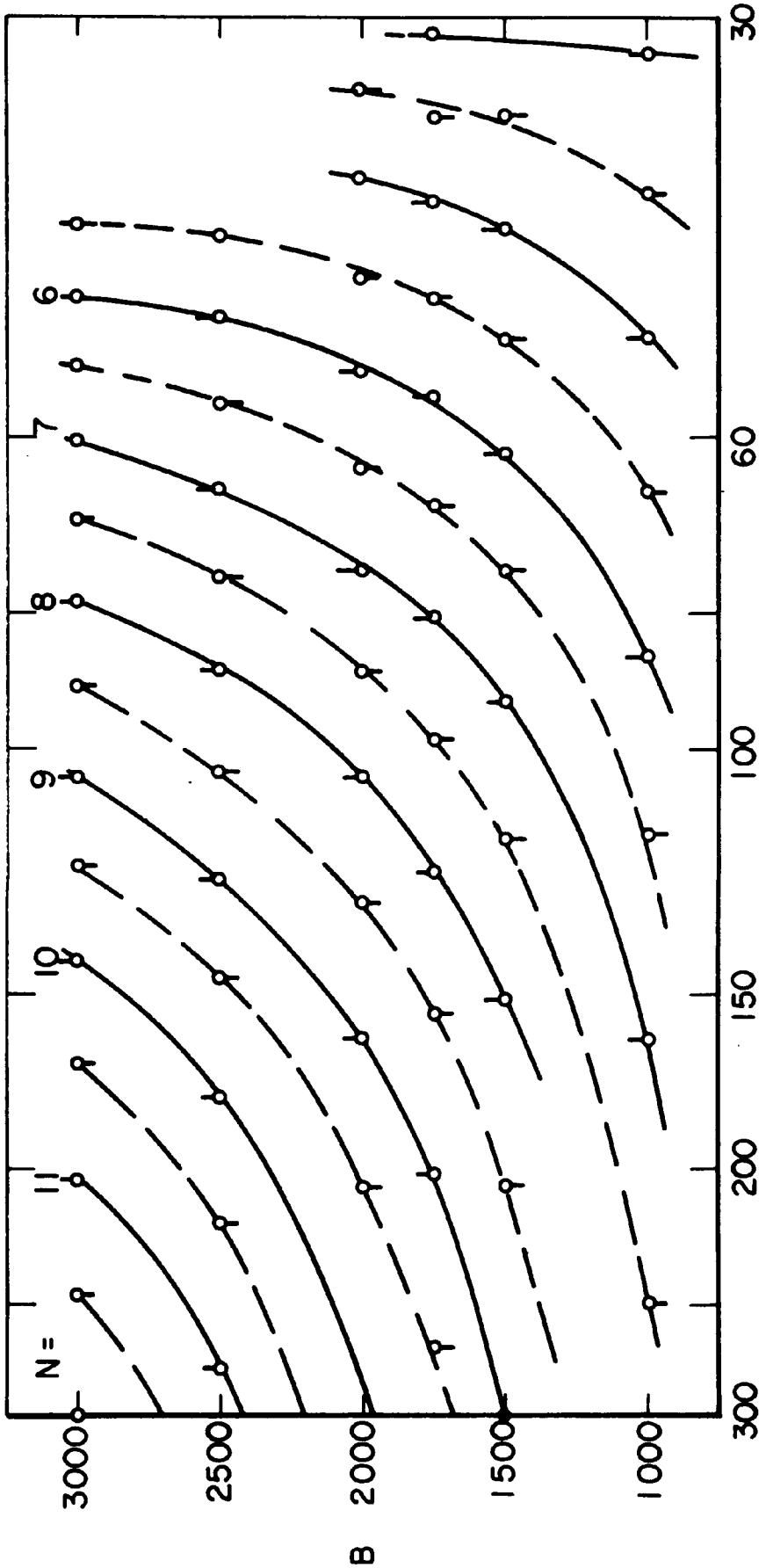


Figure 17. Patterns of the extrema in total cross sections

extrema patterns for each B are arranged vertically, with the ordinate scale proportional to B. Extrema of the same index number are then joined.

2. Comparison of Theory and Experimental Results

The experimental data for the total cross sections are shown in Figures 11 and 12. The precision of the available data does not warrant the detailed comparison of theory and experiment carried out by Rothe, Rol, and Bernstein (1963). Instead, the data are tested for compatibility with the σ and ϵ deduced from the differential cross sections.

In Figure 17, we see that at the lower values of B, the curves become nearly horizontal - - implying a strong dependence of the extrema pattern on the value of B. This strong dependence makes it necessary to use two different extrema patterns to fit the data, one for Li^6 and one for Li^7, with a constant ratio $B_6/B_7 = \mu_6/\mu_7 = 0.862$. From the angular distributions, a σ for each of three possible values of B has been obtained. From the definitions of B and D, we have

$$\epsilon\sigma = \frac{\hbar}{2\mu}\,\frac{B}{\sigma} = \frac{\hbar}{2} D v \quad , \qquad (35)$$

allowing a very approximate value of the product $\epsilon\sigma$ to be obtained for each B. Since the B has been chosen arbitrarily, there will be a corresponding uncertainty in the $\epsilon\sigma$ product; e.g. for the case of B = 1500, a value of B between 1250 and 1750 might yield nearly the same σ , according to the procedure used in analyzing the scattering patterns. Using this trial value of $\epsilon\sigma$ as a guide, semiclassical predictions of the extrema patterns were fitted to the observed extrema-velocities, one pattern being fitted to each isotope for each nominal value of B. Extrema values over a range of B values were used, until a reasonable fit was obtained for both isotopes. From the fit of the experiment to the calculation, a new value of $\epsilon\sigma$ could be estimated. As an example, for the B = 1900 pattern for Li^6, $D_8 = 110$, and

$1/v_8 = 1.51 \times 10^{-5}$ sec cm^{-1} were the values at which a reasonable fit was obtained. From equation 35, this yields the value of $\epsilon\sigma = 3.85 \times 10^{-21}$ erg cm.

Table V gives the values of B, σ, and $\epsilon\sigma$ at which a reasonable fit was obtained between the experimental and calculated extrema patterns. The $\epsilon\sigma$ product obtained from this comparison with the total cross sections may be combined with the σ obtained from the angular distributions to obtain a check value of B:

$$B_{check} = \frac{2\mu}{\hbar^2} (\epsilon\sigma)_{Tot} \cdot \sigma_{Ang} \qquad (36)$$

These check values of B are also included in Table V.

Table V

Parameters Obtained Using Data on Total Cross Sections As Well as Angular Distributions

Li Isotope	B Assumed	σ (Å)	$10^{21}\epsilon\sigma$* (erg cm)	B_{check}
6	900	2.52	1.95	855
6	1380	3.47	2.24	1350
6	1900	2.80	3.85	1880
7	1050	2.52	1.95	1010
7	1600	3.47	2.35	1645
7	2200	2.80	3.95	2240

- - - - - - - -

* Parameters derived considering the two isotopic systems separately; values later averaged. See page 62.

V. Discussion

It has not been possible to determine a unique set of potential parameters for the Li-Hg system due to the problems involved in the fitting of the experimental differential cross section data to theoretical predictions, and to the imprecision of the total cross section data. It has been possible, however, to specify three nearly equivalent sets of parameters (ϵ , σ) which best fit the observations; this effectively limits the range of values of ϵ and σ within which the true values of these parameters most probably lie.

Inspection of the total cross section results indicates that a moderate increase in precision would have been enough to allow the total cross section data to discriminate between the three possibilities for σ afforded by the differential cross section measurements; however, this additional precision was beyond the capability of the present apparatus when used in the crossed beam configuration. It appears that, in order to attain the required precision, the use of a scattering chamber rather than a secondary crossed beam is indicated (see Rothe et al, 1962).

An additional aid in the interpretation of total cross section data might be the relation between the highest index number, N_{max}, assigned to the lowest velocity extremum observed, and the capacity of the well for vibrational energy levels (Bernstein, 1963; Harrison and Bernstein, 1963). Thus any indexing assignment for which $N_{max} > n_o$ (the bound state capacity) could be eliminated. However, this did not aid in the present study; for all proposed assignments, $N_{max} \leq n_o$.

In conjunction with the indexing of the extrema, it is of importance to note that, except for Set 1 at B(nominal) = 1000, different index numbers for Li^6 vs Li^7 had to be assigned to the minimum at lowest velocity, with this minimum for Li^7 requiring an index greater by one than the corresponding minimum for Li^6. Since the experimental curves for the two isotopes are quite similar, it is unlikely that the assignments for the low-velocity minimum would not be the same. This may be taken as an indication that Set 1 at B(nominal) = 1000 is preferred. On the other hand, if the possibility of different index numbers is admitted, then it is possible to rationalize this behavior by consideration of the capacity of the well for bound states. Table VI lists the critical value of B, designated B(crit.), at which a L.-J. (12,6) potential well is just able to contain the v^{th} vibrational level (note that $n_o = v+1$):

Table VI

Vibrational Level Capacity of L.-J. (12,6) Potential Wells
(from Harrison and Bernstein, 1963)

v	7	8	9	10	11	12
B(crit.)	812	1035	1292	1575	1888	2222

For the parameter Sets 2 and 3, corresponding to B(nominal) = 1500 and 2000 respectively, B(crit.) is "bracketed" by the values of B_{check} obtained from the total cross sections. As a result of the increased reduced mass for Li^7, and thus higher B, the Li^7 potential well is capable of containing one more bound state than the Li^6 potential well. For Set 1, this bracketing does not occur, and the capacity of the well is the same for both isotopes. If more precise data were available, the indexing of the extrema could be a useful tool for limiting the choice of acceptable potential parameters.

The angular distribution measurements suffer from the "slope versus spacing" dilemma when comparing experimental and theoretical scattering patterns, as mentioned previously. Although it is possible

that this difficulty might be solved if theoretical scattering patterns were available for B < 1000, the problem is more likely a more basic one, namely a question of the validity of L.-J. (12,6) potential on which the analysis is based (see Mueller and Marchi, 1963).

In Table V, results for the values of $\epsilon\sigma$ were presented which were separately obtained for the particular Li isotope under consideration. Since the electron distribution which determines the interatomic potential is essentially independent of the nuclear properties, the values of $\epsilon\sigma$ determined from each isotopic system were averaged to obtain a "best" set for each nominal value of B. Using these averaged $\epsilon\sigma$ values, values of ϵ (ergs) and ϵ/k (^{o}K) were calculated for each set, and are listed in Table VII.

Table VII

Summary of Experimental Results
(Averages for the Isotopic Systems)

Set	Nominal B	σ (Å)	$10^{21}\epsilon\sigma$ (erg cm)	$10^{14}\epsilon$ (erg)	ϵ/K (^{o}K)
1	1000	2.52	1.95	7.73	560
2	1500	3.47	2.30	6.63	480
3	2000	2.80	3.90	13.9	1008

From a knowledge of the polarizabilities of the atoms involved, it is possible to estimate the C constant for the long range attractive part of the potential. This constant is related to the L.-J. (12,6) potential parameters by equation 21, and to the polarizabilities, α, by

$$C = \frac{3e\hbar}{2\sqrt{m_e}} \frac{\alpha_1 \alpha_2}{\left(\frac{\alpha_1}{N_1}\right)^{\frac{1}{2}} + \left(\frac{\alpha_2}{N_2}\right)^{\frac{1}{2}}} \qquad (37)$$

where N_i is the number of outer shell electrons; e and m_e are the charge and mass of the electron respectively. This is the Slater-Kirkwood relation as used by Rothe and Bernstein (1959). Using the values of

$\alpha_{Hg} = 5.1 \times 10^{-24}$ cm^3, $N_{Hg} = 2$ (Morse and Bernstein, 1962) and $\alpha_{Li} = 22 \times 10^{-24}$ cm^3, $N_{Li} = 1$ (Zorn and Chamberlain, 1963 and Salop, Pollack and Bederson, 1961), C is calculated to be 447×10^{-60} erg cm^6. This value may be compared with "experimental" values obtained from

$$C_{exp} = 4 \sigma_{Ang}^5 (\epsilon\sigma)_{Tot} \qquad (38)$$

The values of C_{exp} calculated in this manner are listed in Table VIII.

Table VIII

Values of C_{exp} Based on Experimental ϵ , σ Values

Set	1	2	3
$10^{60} C_{exp}$ (erg cm^6)	79.2	463	268

The C constant for Set 2 agrees quite well with the theoretically predicted value; however, this must be regarded as fortuitous in view of the very great compounding of experimental errors in evaluating C. In addition, it must be pointed out that this type of comparison has not yielded good agreement in the past for other systems studied. Usually, the experimentally determined C constant has been 1.2 to 2 times larger than theoretical estimates (e.g., see Table III of Rothe, Rol and Bernstein, 1963).

This is the first system for which both extrema in the total cross sections and undulations in the differential cross sections have been observed. In spite of the problems encountered, the methods of analyzing the data allow reasonable limits to be placed on the values of σ and ϵ for the Li-Hg system: $2.5\text{Å} \leq \sigma \leq 3.5\text{Å}$ and $480^\circ\text{K} \leq \epsilon/k \leq 1008^\circ\text{K}$. It is unlikely that in a future experimental determination, the resulting parameters will lie outside these ranges. Even in the face of this limited accuracy, it is possible to draw a meaningful comparison between the Li-Hg system and other related systems studied by the atomic beam scattering technique. For example,

in their studies of the Li-rare gas systems, Rothe, Rol and Bernstein (1963) found values of $\sigma \geq 4.5$Å and values of $\epsilon/k \leq 146^{\circ}$K. The present results indicate a considerably greater depth of the Li-Hg potential well and a significantly smaller equilibrium interatomic separation, implying that the LiHg molecule (thought to be in a $^2\Sigma^+$ electronic state) is more tightly bound than the comparable Li-rare gas di-atom (i.e., "incipient" chemical bonding in LiHg). This possibility is further confirmed by the existence of a known compound, LiHg, observed in connection with studies of the Li-Hg phase diagram (Lyon, 1954).

From experiments on rainbow scattering, Morse and Bernstein (1962) deduced values of the well depth for the K-Hg and Cs-Hg systems. The measurements involved the experimental determination of the energy dependence of the rainbow angle, θ_r. For these systems*, the ϵ/k values were 539°K and 558°K ($\pm$ 7%) respectively. The present ϵ/k values for Li-Hg (Sets 1 and 2) are similar to the results for K- and Cs-Hg. This raises the interesting possibility that the well depth for the alkali-Hg systems may be nearly constant. At present, there are available no theoretical predictions relevant to this question with which the observations may be compared.

- - - - - - - -

* Although σ could not be obtained from their data, values in the range 3.5 to 4.0Å were suggested; these are significantly less than the present results (Table VII) for the Li-Hg system.

VI. Summary

The velocity dependence of the angular distribution of Li scattered by Hg has been measured by the atomic beam technique. Beams of isotopically pure Li^6 and Li^7 were scattered by a crossed beam of Hg. The angular distributions showed evidence of oscillatory deBroglie interferences. By proper selection of the velocity for each of the isotopic Li species, the same deBroglie wavelength could be obtained for the systems Li^6-Hg and Li^7-Hg. The same scattering pattern was observed for the different mass projectiles at constant λ. In addition, the gross angular dependence of the low angle scattering is in accord with predictions based on an assumed long-range inverse sixth power dependence of the attractive potential: $V \sim -C/r^6$. From the comparison of the experimentally observed undulation patterns in the angular distributions (at various relative velocities) with theoretical predictions, assuming a L.-J. (12,6) potential, it was found that σ lies in the range from 2.5 to 3.5Å.

Values of the relative total cross section have also been measured as a function of velocity. The atom-atom impact spectra exhibit extrema, as expected on theoretical grounds. Although these measurements are of marginal precision, they allow a crude determination of the product $\epsilon\sigma$, from which the value of ϵ may be estimated. The values of ϵ/k so determined range from 480 to 1000°K.

The present study indicates that only moderate improvements in molecular beam scattering techniques would yield sufficient precision to enable an "overdetermination" of the L.-J. (12,6) potential parameters for the Li-Hg system. An absolute total cross section and its velocity

dependence should be measured using a scattering chamber containing a known pressure of Hg. This would allow the product $\epsilon\sigma$ to be determined, as well as the long-range C constant. Precise differential cross section measurements should then be performed with the crossed beam configuration; comparison of these measurements with the theoretical scattering patterns would yield a value of σ , for comparison with the value from the total cross section measurements. With sufficiently precise data, it should even be possible to suggest improvements in the form of the potential function.

The present work has emphasized the methodology developed for analyzing scattering data for light-atom systems which exhibit quantum effects. Given more precise data on the velocity dependence of the total and differential elastic scattering cross sections, it should be possible, in the future, to extract potential parameters of high accuracy which could be useful in extending our knowledge of inter-atomic forces.

Appendix A

Phase Shifts Calculated By The Exact Method

Phase shifts were computed by numerical solution of the one dimensional radial wave equation (RKG method) using the IBM 7090 computer at the Computing Center of the University of Michigan or the CDC 1604 computer at the Numerical Analysis Laboratory of the University of Wisconsin. While the concept of the programs used was similar, the details differed considerably. Table IX compares sample phase shifts calculated on the two computers.

Table IX

Comparison of Phase Shifts (in radians)

B	A	ℓ	η_ℓ IBM 7090	η_ℓ CDC 1604
1500	17.32	0	-3.420	-3.420
1500	24.25	0	-12.662	-12.551
1500	24.25	30	16.858	16.851
1000	33.65	0	-26.253	-26.256
1000	33.65	42	10.929	10.920

Tables X a-f summarize all values of phase shifts which were calculated using the exact method. In these tables, a value enclosed in parentheses implies that this value may be uncertain by a multiple of π radians.

Table Xa

Calculated Phase Shifts

B = 1000

A = 17.32		A = 21.00		A = 28.28		A = 33.64	
0	-6.988	0	-11.694	0	-20.324	0	-26.253
3	-2.565	5	-4.471	5	-12.966	5	-18.832
6	+1.417	10	+1.687	10	-6.455	10	-12.148
9	4.953	15	6.739	15	-.822	15	-6.225
15	10.623	20	10.609	20	+3.917	20	-1.069
20	13.798	23	12.312	25	7.692	25	+3.274
22	14.626	25	13.166	30	10.413	30	6.747
23	14.936	28	13.980	33	11.480	33	8.380
24	15.172	31	14.158	37	12.143	35	9.267
25	15.330	32	14.055	38	12.155	37	9.981
26	15.406	33	13.859	39	12.098	38	10.270
27	15.393	34	13.562	40	11.968	40	10.703
28	15.285	36	(12.610)	41	11.756	42	10.929
29	15.074	38	(11.020)	42	11.456	43	10.951
30	(14.747)[a]	39	(6.778)	43	11.058	44	10.919
31	(14.289)	40	(5.086)	44	10.549	45	10.823
32	(13.679)	41	(2.931)	45	9.909	48	10.092
33	(9.747)	42	(2.503)	46	9.108	50	9.157
34	(5.597)	43	(1.907)	47	8.101	53	6.721
35	(3.925)	44	1.623	48	6.772	55	4.505
36	(2.539)	45	1.403	49	4.520	56	3.784
37	2.010	50	.759	50	3.431	58	2.861
38	1.617	55	.455	51	2.861	60	2.269
39	1.351			52	2.460	64	1.530
40	1.150			54	1.899	67	1.180
42	.860			56	1.515	70	.929
44	.662			62	.851	75	.645
50	.336			67	.563	80	.463
55	.206			75	.315	85	.340
60	.133						

- - - - - - - -

[a] These values may be uncertain by one or more π .

Table Xb

Calculated Phase Shifts

B = 1500

A = 17.32		A = 22.00		A = 24.25		A = 27.00	
0	-3.420	0	-9.759	0	-12.664	0	-16.071
3	+1.007	3	-5.286	5	-5.351	3	-11.564
7	6.288	6	-1.142	10	+1.081	6	-7.338
10	9.745	9	+2.640	13	4.485	9	-3.423
13	12.764	12	6.062	17	8.488	12	+.187
16	15.330	15	9.118	20	11.077	15	3.486
19	17.416	18	11.792	23	13.284	18	6.466
22	18.988	21	14.070	27	15.612	21	9.117
25	19.995	24	15.927	30	16.854	24	11.424
26	20.193	27	17.333	33	17.618	27	13.371
27	20.318	29	18.000	35	17.832	30	14.936
28	20.365	30	18.246	38	17.652	32	15.752
29	20.328	31	18.431	40	17.139	34	16.374
30	20.202	32	18.552	42	16.245	35	16.608
31	19.980	33	18.605	43	15.626	36	16.787
32	19.651	34	18.587	44	(14.865)	37	16.910
33	19.205	35	18.494	45	(13.940)	38	16.974
34	18.624	36	18.319	46	(12.793)	39	16.976
35	17.882	37	18.057	47	(11.178)	40	16.912
36	(16.930)	38	17.698	48	(9.779)	41	16.778
37	(15.799)	39	17.233	49	(9.302)	42	16.569
38	(13.848)	40	16.648	50	(2.512)	43	16.279
39	(2.508)	41	15.923	51	(2.162)	44	15.900
40	(1.919)	42	(15.022)	52	(1.891)	45	15.423
41	(1.644)	43	(13.911)	54	(1.487)	46	14.835
42	(1.396)	44	(12.589)	55	1.336	47	14.119
43	(1.202)	45	(3.709)	70	.368	48	(13.248)
44	(1.046)	46	(2.760)			49	(12.174)
45	(.918)	47	(2.299)			50	(10.893)
46	.810	48	(1.964)			51	(5.711)
47	.718	49	(1.707)			52	(3.658)
48	.640	50	(1.499)			53	(3.020)
50	.514	52	1.183			54	(2.584)
55	.313	55	.860			55	2.260
		60	.539			56	2.000
		65	.356			57	1.784
		70	.244			60	1.310
						63	.994
						66	.772
						69	.610
						75	.396

Table Xc

Calculated Phase Shifts

B = 1500

A = 30.00		A = 31.18		A = 32.00		A = 34.64	
0	-19.682	0	-21.085	0	-22.028	0	-25.061
3	-15.160	5	-13.681	3	-17.497	16	-3.668
6	-10.893	10	-6.994	6	-13.208	32	+10.234
9	-6.916	20	+4.029	9	-9.196	35	11.901
12	-3.220	25	8.325	12	-5.449	40	13.920
15	+.191	30	11.743	15	-1.975	42	14.436
18	3.310	35	14.200	18	+1.225	44	14.770
21	6.129	37	14.889	21	4.141	46	14.903
24	8.638	40	15.572	24	6.765	48	14.817
27	10.824	43	15.790	27	9.086	50	14.490
30	12.670	46	15.469	30	11.090	52	13.881
32	13.702	50	13.988	33	12.760	55	12.310
34	14.566	52	12.636	36	14.073	56	11.560
36	15.252	53	(11.745)	39	15.000	57	(10.656)
37	15.524	54	(10.657)	41	15.384	58	(9.555)
38	15.748	55	(9.248)	42	15.501	59	(8.186)
39	15.921	56	(4.563)	43	15.564	60	(5.837)
40	16.041	57	(4.184)	44	15.571	61	(4.463)
41	16.105	58	(3.458)	45	15.519	62	(3.788)
42	16.111	60	(2.642)	46	15.405	63	(3.314)
43	16.056	70	1.039	47	15.223	64	(2.941)
44	15.935			48	14.970		
46	15.479			49	14.638		
48	14.694			50	14.221		
50	13.502			52	13.087		
52	11.759			54	11.438		
53	(10.590)			55	(10.330)		
54	(8.983)			56	(8.942)		
55	(7.428)			57	(7.193)		
56	(3.727)			58	(4.215)		
57	(3.147)			59	(3.522)		
58	(2.742)			60	(3.061)		
60	(2.164)			63	2.175		
65	1.331			66	1.634		
70	.884			70	1.167		
75	.614			75	.804		
80	.440			80	.574		
				85	.421		

Table Xd

Calculated Phase Shifts

B = 1500

A = 51.96		A = 62.35		A = 83.14	
0	-43.572	0	-53.874	0	-73.332
15	-22.400	15	-32.376	20	-44.770
25	-10.826	30	-14.817	40	-21.761
40	+2.459	45	-1.462	60	-4.712
50	8.295	60	+7.165	70	+1.346
55	10.170	70	9.786	85	6.890
60	11.246	73	9.988	90	7.676
62	11.427	75	9.953	95	7.879
65	11.400	77	9.775	100	7.499
67	11.162	80	9.222	105	6.628
70	10.434	85	7.564	110	5.513
75	8.072	90	5.525	120	3.567
80	5.131	95	3.969	130	2.341
90	2.402	100	2.934	140	1.591
100	1.336	105	2.229	150	1.116
115	.643	110	1.729	160	.803
130	.344	115	1.363	170	.591
		120	1.091		
		130	.721		
		140	.494		
		150	.348		

Table Xe

Calculated Phase Shifts

B = 2000

A = 5		A = 10		A = 17		A = 25	
0	21.431	0	11.594	0	.276	0	-10.863
3	25.516	5	18.470	5	7.460	5	-3.527
5	27.697	10	23.670	10	13.509	10	+2.970
10	31.116	15	27.052	15	18.380	15	8.596
12	31.541	20	28.306	20	21.990	20	13.317
15	30.781	25	26.625	25	24.198	25	17.077
17	29.168	28	23.053	30	24.747	30	19.795
18	26.155	29	20.311	35	23.094	35	21.339
19	25.787	30	19.975	38	20.377	40	21.495
20	25.601	31	16.614	39	19.059	45	19.842
21	22.349	32	16.455	40	16.261	50	15.101
22	22.263	33	16.333	41	14.838	51	13.583
23	22.210	34	13.094	42	14.423	52	10.022
24	19.025	35	13.017	43	10.996	53	9.233
25	18.986	37	12.901	44	10.776	54	5.667
26	18.966	38	9.716	45	10.599	55	5.347
27	18.945	39	9.679	46	7.313	56	5.091
28	15.784	40	9.648	48	7.090	57	1.738
31	15.756	41	9.621	49	3.861	58	1.560
32	12.599	42	6.457	50	3.786	59	1.407
45	.006	45	6.405	52	3.663	60	1.274
		46	3.251	53	.472	65	.813
		47	3.240	54	.428	70	.545
		48	3.230	55	.389		
		49	3.221	60	.248		
		50	.072	65	.165		
		55	.044	70	.113		

Table Xf

Calculated Phase Shifts

B = 2000

A = 30		A = 47.58		A = 60.00		A = 80.00	
0	-17.247	0	-37.447	0	-50.431	0	-69.987
10	-3.168	15	-16.372	15	-28.939	20	-41.442
20	+7.886	25	-4.972	30	-11.398	40	-18.481
30	15.671	40	+7.853	45	+1.925	60	-1.524
35	18.191	50	13.220	60	10.503	80	+8.561
40	19.655	55	14.784	65	12.139	85	9.823
45	19.880	58	15.312	68	12.785	88	10.304
50	18.529	60	15.476	70	13.064	90	10.504
56	13.525	62	15.476	72	13.214	92	10.602
57	11.898	65	15.135	75	13.177	95	10.552
58	10.326	67	14.650	77	12.963	97	10.383
59	6.596	70	13.464	80	12.327	100	9.925
60	6.384	72	12.296	85	10.299	105	8.654
61	2.839	75	9.747	90	7.239	110	7.015
62	2.522	78	6.363	100	3.507	120	4.306
70	1.196	80	5.003	110	2.017	130	2.755
80	.580	85	3.217	120	1.260	140	1.851
		90	2.262	135	.683	150	1.289
		100	1.254			160	.925
		110	.758			170	.679
		120	.485			180	.508
		130	.323				

Appendix B

Comparison of Semiclassical and Quantum Total Cross Sections

As mentioned in Section IV.B.1, it is possible to calculate total cross sections from the full quantum treatment or by the semiclassical treatment. Figure 18 compares the cross sections computed by the two methods. The horizontal line represents the Schiff-Landau-Lifschitz total cross section (Bernstein and Kramer, 1963). The vertical bars indicate the position and amplitudes of the extrema, calculated according to the methods outlined by Bernstein (1963). The positions are obtained from the N - 3/8 versus D graphs; the amplitude is estimated using the relation

$$\Delta Q \cong Q_{SLL}\ G(K)\ B^{-0.45} \qquad (B.1)$$

where G (K) is obtained from Figure 7 of the above paper. The points refer to cross sections calculated from the phase shifts, using the partial wave method. These calculations correspond to B = 1500 and A ranging from 17.32 to 83.14. Good agreement is obtained for the locations of the extrema, but the approximated (Equation B.1) amplitudes tend to be too high.

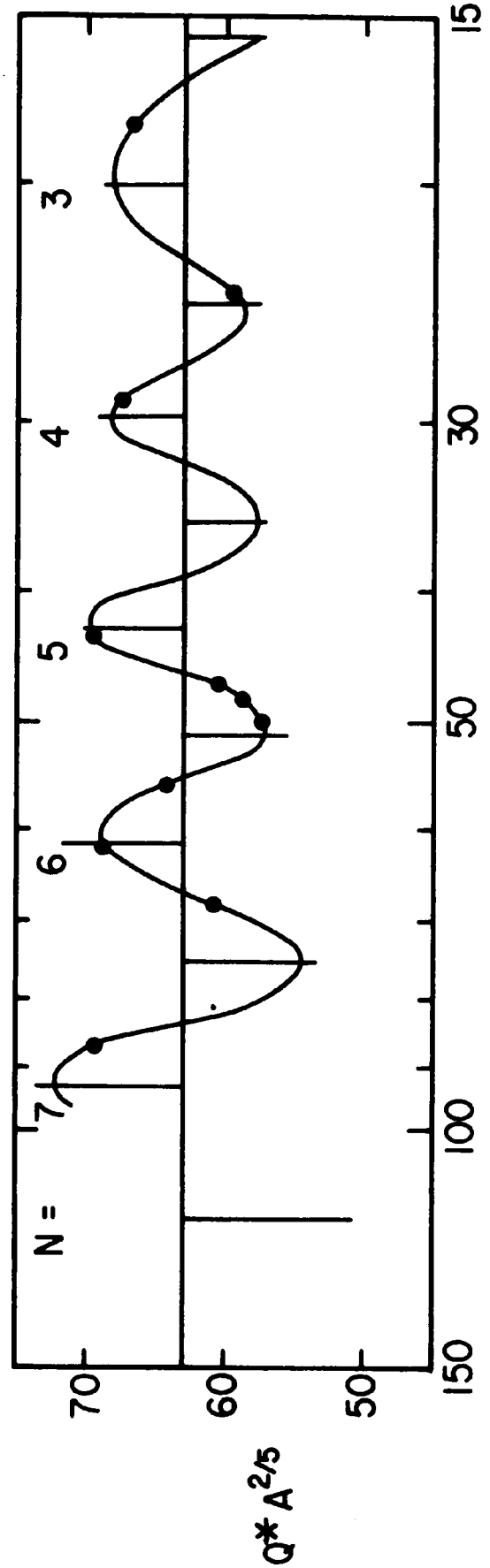


Figure 18. Comparison of semiclassical and quantum cross sections; B = 1500

Appendix C

Transistorized Temperature Regulator

The concentration of Hg atoms at the scattering center depends upon the pressure inside the Hg beam oven, and hence is very sensitive to the temperature of the oven. A transistorized temperature controller was constructed and used to control the temperature of the oven, which is a 100 gm. block of mild steel. The circuit chosen is shown in Figure 19. It follows closely the design of Rachal (1961), which is based upon the design of Garwin (1958). The Null Indicator (NI) is an electronic galvanometer, Model 104W1-G, manufactured by Minneapolis-Honeywell. This instrument has an input resistance of 1,000 ohms, and a voltage sensitivity of better than one microvolt per millimeter deflection of the meter.

A Zener diode-regulated D.C. voltage is applied to a Helipot used as a voltage divider. The variable output of the Helipot is used to buck out the thermal e.m.f. generated by the control thermocouple. The unbalance is sensed by the NI; a signal proportional to the unbalance is taken from the NI, amplified by the 2N43, and used to control the heating current to the oven through the power transistors. The circuit is capable of controlling 200 watts at 24 volts, but is used at a small fraction of its capabilities; the transformer-rectifier power supply in the present model furnishes 3 amp.

Operation of the thermoregulator is straightforward. The load ordinarily consists of two to five ohms of tungsten heater coils. The

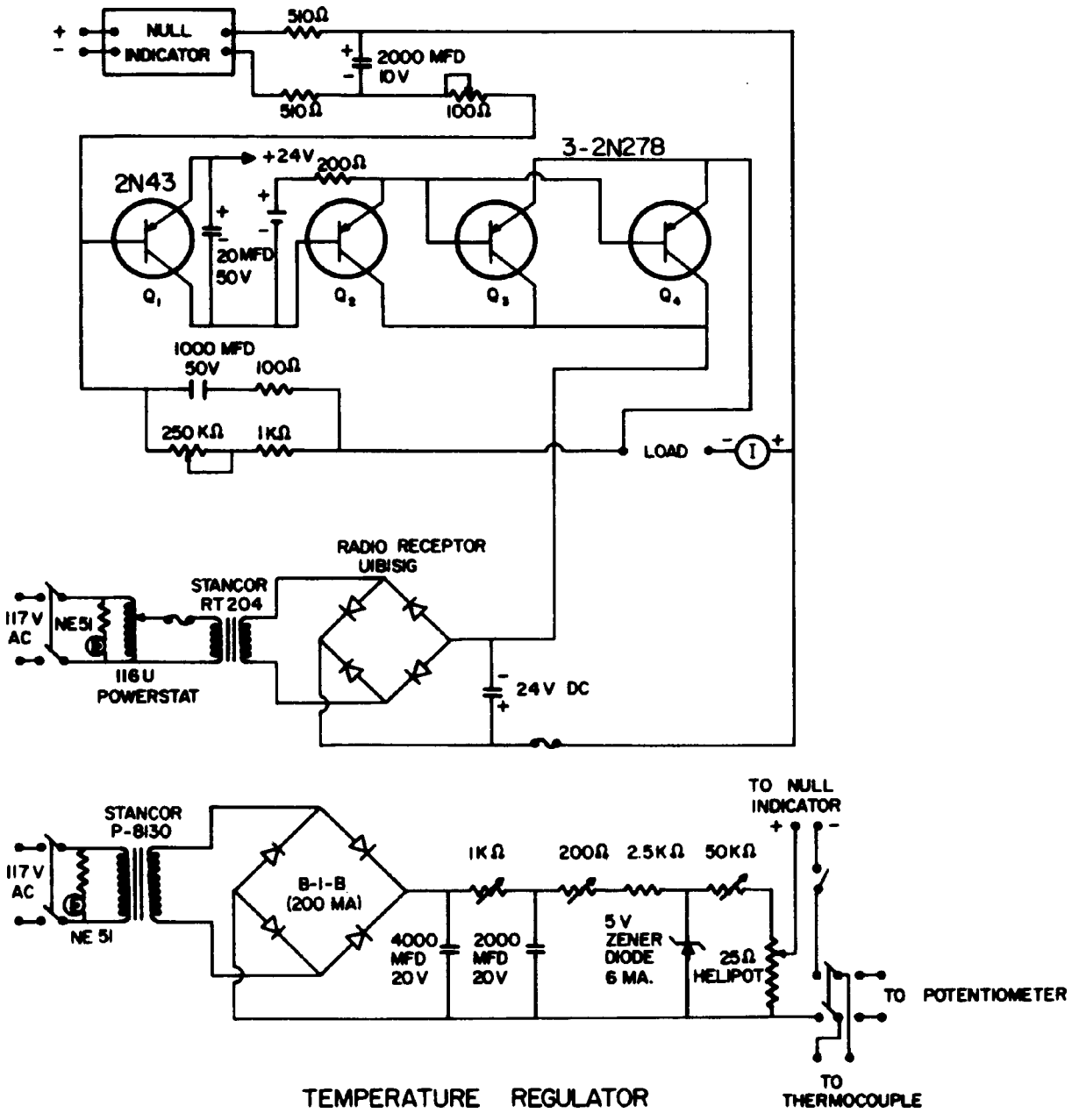

NULL INDICATOR
510Ω
2000 MFD 10V
510Ω
100Ω
3-2N278
+24V
200Ω
2N43
20MFD 50V
Q1
Q2
Q3
Q4
1000 MFD 50V
100Ω
250 KΩ
1KΩ
LOAD
RADIO RECEPTOR UIBISIG
STANCOR RT204
117 V AC
NE51
116U POWERSTAT
24 V DC
TO NULL INDICATOR
STANCOR P-8130
117 V AC
NE 51
B-I-B (200 MA)
1KΩ
200Ω
2.5KΩ
50KΩ
4000 MFD 20V
2000 MFD 20V
5 V ZENER DIODE 6 MA.
25Ω HELIPOT
TO POTENTIOMETER
TO THERMOCOUPLE
TEMPERATURE REGULATOR

Figure 19.

Helipot is adjusted to furnish a voltage corresponding to the desired temperature of operation. (This is conveniently accomplished if the voltage drop accross the 10 turn Helipot is 10 mv.) The NI requires about thirty minutes to warm up and achieve maximum stability; it is zeroed with the input shorted. The D.C. voltage from the power supply is increased until the maximum current passing through the heater is 3 amp. Best regulation however, is obtained if the maximum current available is slightly more than that required to maintain the desired temperature. The 100 ohm sensitivity control and the sensitivity control on the NI are both operated at maximum sensitivity. The power transistors are controlled by a combination of two currents - - one from the NI, and another determined by the 250 K Ω Power Level control. Best performance is obtained by adjusting this control so the current passing through the load, when the input is shorted, is close to the total current required to maintain the desired temperature.

Over periods of several hours, the temperature of the Hg beam oven was maintained constant within limits better than the measuring potentiometer could detect. Since the potentiometer used for observing the temperature had a sensitivity of 10 microvolts, this corresponds to a temperature of 0.25^{o}K, or a variation in the vapor pressure of Hg of about $\pm$1%. In confirmation, it was found that the attenuation of the Li beam was also stable to better than 1% over the entire period of thermoregulation of the Hg oven.

References

K. Berkling, R. Helbing, K. Kramer, H. Pauly, Ch. Schlier and P. Toschek, Zeit. für Physik 166, 406 (1962).

R.B. Bernstein, J. Chem. Phys. 33, 795 (1960).

R.B. Bernstein, J. Chem. Phys. 34, 361 (1961).

R.B. Bernstein, J. Chem. Phys. 37, 1880 (1962).

R.B. Bernstein, J. Chem. Phys. 38, 2599 (1963).

R.B. Bernstein, Proc. Third Int'l. Conf. on Physics of Electronic and Atomic Collisions , London (1963), North-Holland Publ. Co. (In press).

R.B. Bernstein and K.H. Kramer, J. Chem. Phys. 38, 2507 (1963).

W.L. Fite and S. Datz, Ann. Rev. Phys. Chem. 14, 61 (1963).

R.L. Garwin, Rev. Sci. Instr. 29, 223 (1958); erratum, ibid. 29, 900 (1958).

H. Harrison and R.B. Bernstein, J. Chem. Phys. 38, 2135 (1963).

J.O. Hirschfelder, C.F. Curtiss and R.B. Bird, "Molecular Theory of Gases and Liquids", John Wiley and Sons, New York (1954).

H.U. Hostettler and R.B. Bernstein, Rev. Sci. Instr. 31, 872 (1960a).

H.U. Hostettler and R.B. Bernstein, Phys. Rev. Letters, 5, 519 (1960b).

E.H. Kennard, "Kinetic Theory of Gases", McGraw-Hill, New York (1938).

J.G. King and J.R. Zacharias, "Some New Applications and Techniques of Molecular Beams", Chapter I in "Advances in Electronics and Electron Physics", Vol. VIII, L. Marton, editor, Academic Press, Inc. New York (1956).

P. Kusch, "Notes on Resolution in Scattering Measurements", Columbia University, Unpublished (July 21, 1960).

R.N. Lyon, Editor in Chief, "Liquid Metals Handbook", Office of Naval Research, Atomic Energy Commission, U.S. Government Printing Office (1954).

R.E. Minturn, S. Datz and E.H. Taylor, J. Appl. Phys. 31, 876 (1960).

F.A. Morse, Ph.D. dissertation, University of Michigan, Ann Arbor, Michigan, June 1962.

F.A. Morse and R.B. Bernstein, J. Chem. Phys. 37, 2019 (1962).

N.F. Mott and H.S.W. Massey, "The Theory of Atomic Collisions", Clarendon Press, Oxford, England (1949), 2nd edition.

C.R. Mueller and R.P. Marchi, J. Chem. Phys. 38, 745 (1963).

H. Pauly, Fortschritte der Physik 9, 613 (1961).

L.H. Rachal, Rev. Sci. Instr. 32, 940 (1961).

P.K. Rol and E.W. Rothe, Phys. Rev. Letters 9, 494 (1962).

E.W. Rothe and R.B. Bernstein, J. Chem. Phys. 31, 1619 (1959).

E.W. Rothe, P.K. Rol, S.M. Trujillo and R.H. Neynaber, Phys. Rev. 128, 659 (1962).

E.W. Rothe, R.H. Neynaber, B.W. Scott, S.M. Trujillo and P.K. Rol, J. Chem. Phys. 39, 493 (1963).

E.W. Rothe, P.K. Rol and R.B. Bernstein, Phys. Rev. 130, 2333 (1963).

A. Salop, E. Pollack and B. Bederson, Phys. Rev. 124, 1431 (1961).

J.C. Zorn and G.E. Chamberlain, Phys. Rev. 129, 677 (1963).